Radiative heat transfer of non-gray gases in 2D rectangular geometry by ray tracing method and SLW correlated model

Julien Sorel Djeumegni, Myriam Lazard, Vital Le Dez

International Journal of Thermal Sciences 224 (2026) 110739

Contents lists available at ScienceDirect

International Journal of Thermal Sciences

journal homepage: www.elsevier.com/locate/ijts

Radiative heat transfer of non-gray gases in 2D rectangular geometry by ray tracing method and SLW correlated model

Julien Sorel Djeumegni [a,b,*], Myriam Lazard [c], Vital Le Dez [c]

[a] Nantes Université, ONIRIS, CNRS, GEPEA, UMR-6144, 37 Bd de l'université BP406, 44602 Saint-Nazaire, France
[b] Université de Perpignan, PROMES-CNRS, UPR 8521, Tecnosud, Rambla de la thermodynamique, 66100 Perpignan, France
[c] Institut Pprime, Université de Poitiers, CNRS, ENSMA, UPR 3346, 2 Rue Pierre Brousse, Bâtiment B25, TSA 41105, 86073, Poitiers Cedex 9, France

ARTICLE INFO

Keywords:
Radiative heat transfer
Non-gray gases
SLW correlated method
Bickley-Naylor function
Planck-mean

ABSTRACT

The ray-tracing method and the SLW correlated model have been implemented to address the problem of radiative heat transfer in a two-dimensional geometry filled with non-gray gases. Mixtures with 10%CO_2 and 20%H_2O were treated as the participating non-gray gases, while N_2 was regarded as non-participating in the radiative transfer process. The SLW correlated method has been used to compute discrete absorption coefficients, their associated weights, and the Planck-mean absorption coefficient. An exact semi-analytical method using Bickley-Naylor functions, Gauss quadrature, and the ray tracing method has been developed to solve the radiative transfer equation (RTE). Radiative properties of the non-gray gases have been calculated for different temperatures to describe the thermal behavior of the medium. The effect of the reference temperature and non-gray gas radiative properties on the RTE integral solutions, was also examined. Dimensionless temperature and radiative heat flux distributions were simulated and tabulated under radiative equilibrium, then presented and discussed. The computed radiative quantities showed good agreement with established reference models.

Nomenclature

a_g	weighted coefficients of discrete gray gases
C_{abs}	prescribed absorption cross section
C_{max}	maximum absorption cross section
C_{min}	minimum absorption cross section
$\widetilde{C}_g$	supplemental absorption cross section
C_η	spectral absorption cross section
C^Ω	unit disk of $\mathbb{R}^2 : C^\Omega = \{\Omega \in \mathbb{R}^2 \,/\, \lvert\Omega\rvert \leq 1\}$
$\left(\vec{e}_x, \vec{e}_y\right)$	unit vectors of x, y directions
g	gray gas number
G	volumic incident radiation $\left(Wm^{-3}\right)$
G_g	volumic incident radiation of a discrete gray gas $\left(Wm^{-3}\right)$
G^*	dimensionless incident radiation
H_x, H_y	length of the rectangular section along x and y direction (m)
(i,j,p,q)	cells numbering
I	incoming radiation intensity $\left(Wm^{-2}Sr\right)$
I_b	black body radiation intensity $\left(Wm^{-2}Sr\right)$
k_η	spectral absorption coefficients $\left(cm^{-1}\right)$
k_g	discrete absorption coefficient $\left(m^{-1}\right)$
Ki_n	Bickley-Naylor functions

(*continued on next column*)

(*continued*)

l, m	angular and spatial numbering quadrature
N_g	total number of discrete gray gases
M_φ, N_θ	number of angular quadrature
N_x, N_y	number of cells of the mesh grid
P_T	total pressure at which gas characteristics are evaluated (Pa)
$\overrightarrow{q}^r$	radiative flux vector $\left(Wm^{-2}\right)$
$\overrightarrow{q}^{r^*}$	dimensionless radiative flux vector
$\overrightarrow{S}^r$	radiative source vector $\left(Wm^{-3}\right)$
s	curvilinear abscissa (m)
T_E, T_N, T_W, T_S	prescribed temperature at East, North, West, and South walls (K)
T	radiation temperature in the medium (K)
T_0	initial temperature in the medium (K)
T_{hot}	hot temperature at wall (K)
T^{ref}, T_b	reference temperature (K)
T_g	temperature at which the gas properties are calculated (K)
T^*	dimensionless temperature in the medium
u	real number at which $E(u)$ is evaluated
Y_s	chemical ratio of absorbing gases
Subscripts	
$\partial\mathscr{D}_e$	bounded domain of the geometry section
$\{\mathscr{D}_i\}$	participating domain of the geometry section $\mathbb{R}^2$
$\{\mathscr{D}\}$	entire domain of the geometry section $\mathbb{R}^2$

* Corresponding author. Nantes Université, ONIRIS, CNRS, GEPEA, UMR-6144, 37 Bd de l'université BP406, 44602 Saint-Nazaire, France.
E-mail address: julien.djeumegni@univ-nantes.fr (J.S. Djeumegni).

https://doi.org/10.1016/j.ijthermalsci.2026.110739
Received 3 September 2025; Received in revised form 19 December 2025; Accepted 28 January 2026

1. Introduction

Radiative heat transfer in participating non-gray gases at high temperatures plays a crucial role in many industrial processes and engineering applications, including combustion chambers, aircraft and aerospace systems, rocket engines, furnaces, and nuclear power equipment [1]. Variations in the radiative spectral bands of non-gray gases significantly affect both the temperature distribution and the exchanged radiative heat flux [2,3]. In addition, the geometry of the participating medium and the radiation path length interacting with molecular gases influence the overall energy balance [4]. For participating gases containing particles such as soot or droplets, radiative transfer occurs through the absorption, emission, and scattering of photons by both gas species and particles. Consequently, carbon dioxide (CO_2) and water vapor (H_2O) remain the most extensively studied participating gases due to their practical relevance in many applications [5]. The present work focuses on radiative heat transfer coupled with the kinetics of non-gray gases within a two-dimensional geometry. The key radiative properties of interest are the absorption coefficients of non-gray gases, which are derived from their absorption spectral bands.

To date, the need to obtain exact analytical or semi-analytical solutions for radiative transfer coupled with the kinetics of non-gray gases remains significant. However, the integro-differential nature of the radiative transfer equation (RTE) results in increased computational complexity [3]. Moreover, the strong temperature dependence of the radiative spectral properties of non-gray gases further complicates its solution [4]. Based on the literature, numerical methods have been extensively employed to investigate radiative transfer in non-gray gases, particularly in multidimensional configurations. Among these studies, Goutiere et al. [6] performed a two-dimensional evaluation of seven real-gas models for carbon dioxide (CO_2) and water vapor (H_2O), including the cumulative-k (CK), statistical narrow-band (SNB), hybrid SNB-CK, gray-band (GB), weighted sum of gray gases (WSGG), spectral line-based weighted sum of gray gases (SLW), and exponential wide-band (EWB) methods. Five test cases were examined, encompassing homogeneous and non-homogeneous, isothermal and non-isothermal conditions for both single gases and gas mixtures. The results indicated that the SNB and SNB-CK methods offer the highest accuracy, while the SLW method provides the best compromise between accuracy and computational cost. In a subsequent study, Goutiere et al. [7] compared the accuracy and computational efficiency of five real-gas methods for radiative heat transfer prediction in one- and two-dimensional enclosures. The analysis included the CK method, three hybrid SNB-CK variants, and the SLW method, with particular emphasis on the hybrid SNB-CK approaches, which achieved accurate predictions with significantly reduced computational time compared to the original SNB-CK model. In a similar context, Chu et al. [8] investigated radiative heat transfer in a two-dimensional rectangular enclosure containing $CO_2/H_2O/N_2$ gas mixtures. For the non-gray gases, the authors employed the line-by-line (LBL) model as described in Refs. [9,10], based on the updated HITEMP2010 spectroscopic database [11], and the SNB-CK model proposed by Soufiani and Taine [12]. The radiative transfer equation (RTE) was solved using the discrete ordinates method (DOM) with the T_7 quadrature scheme. Five test cases involving participating gases CO_2/N_2, H_2O/N_2, and $CO_2/H_2O/N_2$ were examined. The results obtained with the SNB-CK model showed good agreement with the LBL model across all test cases. Hence, the SNB-CK model can serve as a benchmark when LBL calculations become computationally prohibitive, particularly for multidimensional geometries. Cherifi et al. [13] further developed a two-dimensional radiation code based on the discrete ordinates method combined with the SLW model for non-gray absorbing-emitting gases. The model was analysed for use in conjunction with computational fluid dynamics (CFD) simulations. Using the same test cases proposed by Goutiere et al. [6], the predicted radiative source terms and radiative heat fluxes exhibited good accuracy. Turning to Amiri and Lari [14], they evaluated the full-spectrum k-distribution (FSK) and SLW models for homogeneous and non-homogeneous mixtures of carbon dioxide and water vapor. The results were benchmarked against line-by-line (LBL) model predictions. The radiative transfer equation was solved at radiative equilibrium, using the discrete ordinates method and the finite volume method (FVM) for angular and spatial discretisation, respectively. Six test cases were considered to assess the accuracy and computational efficiency of the gas radiation models. The results demonstrated that the gray-Planck model was the only approach that failed to provide accurate predictions. In addition, Sun et al. [15] investigated combined conduction-radiation heat transfer in non-gray gases within a two-dimensional enclosure. The energy and radiative transfer equations were solved using the finite volume method, and the spectral properties of CO_2, H_2O, and CO were analysed using the SLW model. The effects of gas species, mixture composition, and wall emissivity on radiative quantities were examined. The results showed that the P1 approximation led to significant errors in temperature and heat flux predictions, as well as overprediction of radiative integrals. Beyond two-dimensional analyses, comparable investigations have been conducted in three-dimensional geometries. So, Yang et al. [16] analysed radiative transfer involving non-gray gases and particles in a three-dimensional combustion system using the DRESOR and SNB-CK approaches. Radiative heat fluxes, source terms, and radiative intensities at different directional resolutions were computed using the DRESOR and DOM in conjunction with the SNB-CK model. Absorbing-emitting and scattering non-gray gases were considered to assess the accuracy of the DRESOR method. On the other hands, Numerical simulations of radiative transfer with non-gray gases in 3D enclosures were extended by Coelho et al. [17] using DOM and DTM. Following the evaluation of different radiative property models, the CK model was found to be highly efficient, yet it requires significant computational time.

The literature review demonstrates that exact semi-analytical and ray-tracing methods have not yet been extended to non-gray gas radiation in two-dimensional geometries. However, many thermal engineering applications involving non-gray gases require computationally efficient solution methods. To address this need, a correlated SLW model

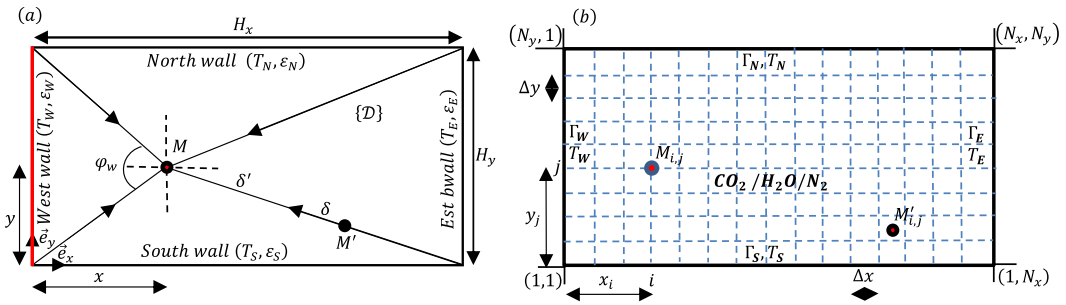

Fig. 1. Rectangular section of the participating medium, filled by non-gray gases $CO_2/H_2O/N_2$: (*a*) Ray path length from radiation to point M, (*b*) mesh grid.

is developed and combined with a ray-tracing method. The real gas model is based on an updated correlation of the absorption-line blackbody distribution function (ALBDF), proposed by Pearson et al. [18,19], using the HITEMP2010 spectroscopic database [11]. Its compatibility with the ray-tracing method used to solve the radiative transfer equation motivates the present study.

The study focuses on computing absorption coefficients of CO_2, H_2O and their mixture using the SLW correlated model and integrate these results to solve the RTE in a 2D rectangular geometry. Thus, the discrete gray absorption coefficients and their respective weights are correlated following Pearson et al. [19]. The exact semi-analytical solutions of the radiative source, following Refs. [20,21] have been validated for a constant temperature within the medium. Temperature and heat flux distributions inside the two-dimensional geometry are computed at equilibrium, using the specific Bickley Naylor functions [22]. Then, the numerical results of dimensionless temperature and heat flux distributions in the 2D geometry are presented as curves, tables, and numerical simulations.

2. Geometry

Let's consider a rectangular section depicted in Fig. 1(a and b), containing a semi-transparent non-gray gas such as carbon dioxide (CO_2), water vapor (H_2O) and Nitrogen (N_2) or their mixture. Nitrogen species is a spectral window and consequently doesn't absorb radiations. Only kinetic concentrations of gases are considered, disregarding the velocity and flow characteristics. The radiative problem is solved in the (x,y) frame using unit vectors $\vec{e}_x$ and $\vec{e}_y$ along the axes. The gas flame starts at T_0 and propagates in the $\left(\vec{e}_x, \vec{e}_y\right)$ plane, with the z-axis assumed infinite, resulting in no variation of thermal quantities along this direction. Due to strong geometric variations in thermal radiation, ray path lengths are studied before solving the radiative transfer equation combined with gas properties. The geometry presented in Fig. 1(a and b) illustrates a rectangular section with dimensions $H_x \times H_y$ in the (x,y) coordinate system, which physically represents a burner. The participating domain $\{\mathscr{D}_i\}$ of the radiative problem is given by Eq. (1) below:

$$\{\mathscr{D}_i\} = \left\{\forall (x,y) \in \left]0, H_x\right[\cap \left]0, H_y\right[\right\}, \tag{1}$$

with boundaries surfaces denoted by $\partial\mathscr{D}_e \in \{\Gamma_E \cup \Gamma_W \cup \Gamma_N \cup \Gamma_S\}$, which are subjected to the constant temperatures T_E, T_W, T_N, T_S, respectively.

Therefore, the semi-transparent gaseous medium is enclosed within the entire domain $\{\mathscr{D}\} \in \partial\mathscr{D}_e \cup \{\mathscr{D}_i\}$. An isothermal mesh grid with uniform spacing $\Delta x \times \Delta y$, where $\Delta x = H_x/(N_x - 1)$ and $\Delta y = H_y/(N_y - 1)$, is used to discretise the spatial coordinates of the point $M(x,y)$, following the finite difference method. Then, a numerical evaluation of the radiative quantities is carried out at the node positions $\left(x_i, y_j\right)$, where $(i,j) \in [2, N_x - 1] \times [2, N_y - 1]$.

3. Ray tracing formulation

The ray-tracing method is presently applied to thermal radiation to evaluate the ray path length of the hot gases within the geometric domain. Thermal rays propagate along a direction vector $\vec{\Omega} = \begin{pmatrix} \cos\varphi \sin\theta \\ \sin\varphi \sin\theta \\ \cos\theta = 0 \end{pmatrix}$, where φ and θ denote the azimuth and zenith angles, respectively with $\varphi \in [0, 2\pi]$ and $\theta \in [0, \pi]$. To compute the radiative integral solutions of the RTE for all calculation points $M(x,y) \in \{\mathscr{D}\}$ inside the medium, the thermal rays follow two types of optical pathways. The first type originates from any hot wall on $\partial\mathscr{D}_e$ at temperature T_{hot} and follows a path of length δ, such that $\overrightarrow{M_{\partial\mathscr{D}_e}M} = \delta\vec{\Omega}$. For the present geometric configuration shown on Fig. 1-(a), the hot wall is located at the West boundary (Γ_W), where hot gases enter the burner. Therefore, the ray path length propagating from that boundary into the medium is given by $\delta = -x/\cos\varphi_w \sin\theta$. The second pathway originates from any radiative source point belonging to the medium $M'(x',y') \in \{\mathscr{D}_i\}$ to the calculation point $M(x,y)$, such that $\overrightarrow{M'_{\mathscr{D}_i}M} = \delta'\vec{\Omega}$, where $\delta' = (x' - x)/\cos\varphi_w \sin\theta$ in the (x,y) plane, and depends on the weighted positions $\delta_k \in [0, 1]$. Incident radiation, temperature, and radiative heat flux distributions are then computed at the center of each mesh cell, identified by the node (i,j). From any source point $M'\left(x'_i, y'_j\right) \in \{\mathscr{D}_i\}$ belonging to Γ_W and covered by φ_w, the corresponding relations $x'_i = (1 - \delta_k)x_i = f_1(x_i)$ and $y'_j = y_j \pm \delta_k x_i \tan\varphi_w = f_2\left(y_j\right)$ are used. To facilitate numerical computations, the Cartesian coordinates of $M'\left(x'_i, y'_j\right)$ are converted into discretised integers (p,q) using the relations $x_p - \Delta x \le x'_i \le x_p + \Delta x$ and $y_q - \Delta y \le y'_j \le y_q + \Delta y$. Due to the respective spatial dependence of $x'_i = f_1(x_i)$ and $y'_j = f_2\left(y_j\right)$, the integers labelled by (p,q) in terms of nodes (i,j) therefore follow the mathematical relation given by Eq. (2).

$$\begin{cases} p = E\left[\left(i + \dfrac{1}{2}\right) - \left(i - \dfrac{3}{2}\right)\delta_k\right] \\ q = E\left[\left(j + \dfrac{1}{2}\right) \pm \left(i - \dfrac{3}{2}\right)\delta_k \tan\varphi_w\right] \end{cases}, \tag{2}$$

where, $E(u)$ denotes the integer part of a real number $u \in \mathbb{R}$. A similar methodology is applied to all the walls with $\varphi \in [0, 2\pi]$, to solve the radiative problem.

4. Governing equations

4.1. Spectral line-based weighted-sum-of-gray-gases model (SLW)

Absorption coefficients will be reordered into sets of absorbing bands or discrete gases before being combined with radiative transfer calculations, due to the direct dependence of the participating gases on the spectral wavelength. The SLW model uses a combination of the WSGG model [17] and gray gas coefficients k_j and a_j defined by Hottel and Sarofim [23]. It uses the ALBDF [24], defined as the fraction of blackbody energy in specific portions of the spectrum, with the absorption cross section given by $F\left(C_{abs}, T_b, T_g, P_T, Y_s\right)$. It enables the evaluation of the weighted coefficients a_j in the medium and at the boundaries. The function $F\left(C_{abs}, T_b, T_g, P_T, Y_s\right)$ is calculated from the high-resolution absorption coefficients spectrum. It depends on the absorption cross section C_η, the blackbody temperature T_b, the gas temperature T_g, the total pressure P_T, and the molar fraction of the relevant gas Y_s. The SLW model uses these variables as its relevant tools because it quantifies a weighted portion of the absorption coefficients spectrum according to the Planck emissive power, ensuring that it remains below the prescribed value of C_{abs}. Therefore, it is given by Eq. (3) below:

$$F\left(C_{abs}, T_b, T_g, P_T, Y_s\right) = \frac{1}{\sigma T^4} \int_{\left\{\eta : C_\eta\left(T_g, P_T, Y_s\right) \le C_{abs}\right\}} E_{b\eta}(\eta, T_b) d\eta, \tag{3}$$

where, the subscript i denotes the i^{th} spectral interval, and the summation is performed over the entire spectrum η. From the line-by-line integration over the spectrum, the SLW model divides the entire wavelength range into a set of absorption cross sections $\widetilde{C}_g$ for $0 \le g \le N_g$. The supplemental absorption coefficient is selected between its minimum $\widetilde{C}_0 = C_{min}$ and maximum $\widetilde{C}_{N_g} = C_{max}$ values, as described in Eq. (4).

$$\widetilde{C}_g = C_{min}\left(\frac{C_{max}}{C_{min}}\right)^{\frac{g}{N_g}}, 0 \le j \le N_g, \tag{4}$$

where N_g is the total number of discrete gray gases. The computations of ALBDF using the update HITEMP-2010 line-by-line data [19] are performed within a spectral interval $\Delta\eta$ and compared with the prescribed value C_{abs}. The Planck blackbody energies within $\Delta\eta$ have been summed and the result at a given temperature T_b has been divided by the emissive power. Starting from the original hyperbolic tangent form of ALBDF [24], the updated correlation proposed by Pearson et al. [19] yields more accurate results, after performing least-squares curve fitting. This methodology is currently used as part of the SLW correlated method applied to non-gray gases. The absorption cross section functions of CO_2, and H_2O at atmospheric pressure are exhibited in Appendix. A. Additionally, the classical approach of Denisson and Webb [25] has been refined using the modified method of Darbandi and Abrar [26] for the present analysis, because of the high sensitivity of gas temperature in non-isothermal combustion. Finally, the discrete absorption coefficients and their associated weights, integrated into the RTE solver, are derived from both the correlated ALBDF and modified reference approaches. In the modified reference approach, the black-body temperature is set to the local temperature, $T_b = T^{loc}$, and the gas temperature is used as the reference temperature, $T_g = T^{ref}$. Both parameters are used in evaluating the discrete absorption coefficients, $k_g = k_g^{loc}$ of gray gases, computed according to Eq. (5).

$$k_g = NY_s\left(\widetilde{C}_{g-1}\widetilde{C}_g\right)^{\frac{1}{2}}, \tag{5}$$

where $N = \frac{P_T}{R_u T_g}$, with R_u denoting the ideal gas constant. Therefore, the modified absorption cross section satisfies $\widetilde{C}_g = \widetilde{C}_g^{loc} = \widetilde{C}_g^{ref}$. The weighted gray gases coefficients, $a_g = a^{loc}$ are then calculated according to Ref. [26] using Eq. (6):

$$a_g = F\left(\widetilde{C}_g^{ref}, T_g = T^{ref}, T_b = T^{loc}\right) - F\left(\widetilde{C}_{g-1}^{ref}, T_g = T^{ref}, T_b = T^{loc}\right). \tag{6}$$

For homogeneous flame gases burning at isothermal temperature T_g, the wavenumber interval Δ_g of the discrete gray gas is computed from intersection of the discretised cross section $\widetilde{C}_g$ and the spectral cross section $C_\eta(T_g, Y_s)$. The relations given by Eq. (7) and Eq. (8) illustrate the case.

$$\Delta_g = \left\{\eta : \widetilde{C}_{g-1} \le C_\eta(T_g, Y_s) \le \widetilde{C}_g\right\}, \text{gray gas } g \tag{7}$$

$$\Delta_0 = \left\{\eta : C_\eta(T_g, Y_s) \le \widetilde{C}_0\right\}, \text{clear gas}. \tag{8}$$

For non-gray gases that exhibit significant heterogeneity under non-isothermal conditions, the reference conditions approach has been developed, using a fixed spectral integration interval throughout the participating medium. After evaluating the gray gas parameters k_g and a_g, the radiative transfer equation is applied to compute the resulting radiative quantities. In the present analysis, both the absorption coefficients and their corresponding weighted coefficients are functions of the medium temperature, $T(x, y)$ such that $T_g = T_g^{ref}$ and $T_b = T_g^{loc} = T(x, y)$. The radiative properties in the current SLW correlated method are computed using the updated correlated kinetic equations presented by Pearson et al. [19] (see Appendix. A). A new set of coefficients has been added to better represent the ALBDF at a pressure of $1atm$. Carbon dioxide coefficients are independent of mole fraction, while water vapor coefficients include self-broadening effects. These coefficients are valid for temperatures between $400K \le T_g, T_b \le 3000K$, and pressures from of $0.1atm \le P \le 50atm$. A value of $10^{-4} m^2/mol$ is recommended for C_{min} for both CO_2 and H_2O gas species, whereas C_{max} is suggested $600 m^2/mol$ for CO_2 and $60 m^2/mol$ for H_2O. In two-dimensional geometry, variations in gas temperature across the (x, y) plane lead to corresponding variations in absorption and weighted coefficients. The geometry considered in this work includes system containing either a single gas (CO_2 / N_2 or H_2O/ N_2) or a gas mixture (CO_2 /H_2O/N_2). For gas mixtures of CO_2 /H_2O/N_2 burning in the medium, the corresponding absorption and weighted coefficients are given by $k_g^{mix} = k_g^{(CO_2)} + k_g^{(H_2O)}$ and $a_g^{mix} = a_g^{(CO_2)}.a_g^{(H_2O)}$. Since the purpose of evaluating the radiative properties of participating non-gray gases is based the ALBDF, the Planck-mean absorption coefficient will also be derived.

4.2. Planck-mean absorption coefficient

Abrupt spectral variations in absorption coefficients of molecular gases, complicate the computation of the radiative transfer equation. Introduction of the Planck-mean absorption coefficient accurately describes radiative heat losses or the total emission from the participating gas [27]. It relies on line-by-line calculations from the high-precision HITEMP [11,28] and HITRAN [29] databases. It has been applied to scale absorption coefficients in various radiation models, including the full-spectrum correlated-k (FSCK) [30] and the multi-scale full-spectrum correlated-k (MSFSCK) [31]. In the current SLW correlated formulation, the Planck-mean absorption coefficient is scaled with the high-resolution HITEMP-2010 database [11]. The Planck-mean absorption coefficient κ_p, is defined mathematically following Eq. (9):

$$\kappa_p = \frac{\int_0^\infty k_\eta I_{b\eta} d\eta}{\int_0^\infty I_{b\eta} d\eta} = \frac{1}{I_b}\int_0^\infty k_\eta I_{b\eta} d\eta, \tag{9}$$

where $I_b = \frac{\sigma_B T^4}{\pi}$ represents the total blackbody intensity, while $I_{b\eta}$ and k_η denote the spectral blackbody intensity and spectral absorption coefficient, respectively. Since, κ_p represents the contribution of each spectral line, it varies smoothly across the spectrum, as described by the HITEMP-2010 database. Thus, κ_p can be expressed as a sum of weighted coefficients across the entire absorbing-emitting spectrum of the participating gases. From Eq. (9) one can derive Eq. (10):

$$\kappa_p = \frac{1}{I_b}\sum_i I_{b\eta_i}\int_0^\infty k_{\eta_i} d\eta = \frac{\sum_i I_{b\eta_i}}{I_b} S_i \tag{10}$$

where $S_i = \int_0^\infty k_{\eta_i} d\eta$ is the line strength, or line-integrated coefficient. The SLW formulation, which scales the Planck-mean absorption coefficient, is derived from the ALBDF set in Eq. (3). Each gray gas g represents the contribution of an individual spectral line. So, the Planck-mean set in Eq. (11) is defined as the product of the absorption coefficients k_g and weighting coefficients a_g for each gray gas within the spectral interval [2,4].

$$\kappa_p = \sum_{g=0}^{N_g} a_g k_g. \tag{11}$$

If the medium contains a mixture of participating gases, Eq. (11) is modified as shown in Eq. (12) below:

$$\kappa_p^{mix} = \sum_{g=0}^{N_g} a_g^{mix} k_g^{mix}. \tag{12}$$

The line strength S_i is evaluated with its pressure and temperature dependence included in the ALBDF calculation.

4.3. Spectral formulation of thermal radiative transfer

Radiative heat transfer is analysed within the rectangular section, where the gases burn under steady-state conditions. The semi-transparent medium is absorbing-emitting, non-scattering and bounded by black surfaces along $\partial\mathscr{D}_e$. In combustion applications involving semi-transparent gases, thermal propagation (∂t) is significantly faster than the thermal response (∂I_η). Consequently, the temperature field varies slowly in time, such that $(\partial I_\eta / \partial t \approx 0)$. The steady-state spectral radiative transfer equation is given in Eq. (13) below:

$$\vec{\Omega}.\vec{\nabla}I_\eta\left(s,\vec{\Omega}\right) = -\kappa_\eta\left\{I_\eta\left(s,\vec{\Omega}\right) - n^2 I_{b\eta}[T(s)]\right\}. \quad (13)$$

Here, I_η is the spectral radiative intensity, κ_η is a spectral absorption coefficient, n the unit refractive index, $I_{b\eta}$ the spectral Planck radiative intensity, T the temperature in the medium, s the curvilinear abscissa and $\vec{\Omega}$ the unit propagation direction. Due to the integro-differential formulation of the RTE, boundary conditions are required. For a wall position s_w and direction $\vec{\Omega}$ at a given time t, the condition is specified in Eq. (14):

$$I_\eta\left(s,\vec{\Omega}\right) = I_{b\eta}[T(s_w)]\ \left(s,\vec{\Omega}\right) \in \partial\mathscr{D}_e \times \Theta^\Omega, \quad (14)$$

In the (x,y) coordinate system with unit refractive index, Eq. (13) reduces to Eq. (15):

$$\sin\theta\cos\varphi\frac{\partial I_\eta(x,y,\theta,\varphi)}{\partial x} + \sin\theta\sin\varphi\frac{\partial I_\eta(x,y,\theta,\varphi)}{\partial y} = -\kappa_\eta I_\eta(x,y,\theta,\varphi) + \kappa_\eta I_{b\eta}[T(x,y)]. \quad (15)$$

The spectral dependence of absorption coefficients, radiative intensity, and the Planck radiative intensity introduces significant complexity to accurately predicting gas heat transfer within the geometry. To overcome this issue, absorption coefficients are subsequently reordered into a set of absorbing bands. Thus, Eq. (15) is solved across the full spectral band $\eta \in [0,+\infty[$ by dividing the participating medium into N spectral intervals of width $\Delta\eta$, with $\eta = N\Delta\eta$. To reduce computational resources while preserving accuracy, the SLW method as described in Refs. [19,25,26] converts the full spectral dependence of gases into discrete gray bands.

4.4. Radiative heat transfer equation combined with SLW correlated model

The SLW correlated model is combined with the RTE by transforming the spectral dependence of the incoming radiation I_η across the entire absorption band of the radiative gas. The RTE is therefore solved for each discrete gray gas contributing to the absorption spectral band. So, let us consider a semi-transparent medium discretised into N_g participating gray gases, as studied in the SLW model [19] for a one-dimensional slab, according to Eqs. (5) and (6).

For each spectral width $\Delta\eta$ of a gas absorption band, the radiative intensity is expressed as the sum of contributions from the discrete gray gases I_g, according to Eq. (16):

$$\sin\theta\cos\varphi\frac{\partial I_g(x,y,\theta,\varphi)}{\partial x} + \sin\theta\sin\varphi\frac{\partial I_g(x,y,\theta,\varphi)}{\partial y} = k_g\left[I_{b_g}[T(x,y)] - I_g(x,y,\theta,\varphi)\right], \quad (16)$$

subjected to boundary conditions following Eq. (17):

$$I_g(x,y,\theta,\varphi) = a_g[T_w]I_b[T_w], (x,y) \in \partial\mathscr{D}_e, (\theta,\varphi) \in \Theta^\Omega, g \in \left[1,N_g\right]. \quad (17)$$

$I_{b_g} = a_g I_b$, with $I_b = \frac{\sigma_B T^4}{\pi}$ and T_w represents the temperature at walls.

For a spectral window corresponding to a clear or transparent gas ($g = 0$), with $k_0 = 0$ and $a_0 \neq 0$, Eq. (16) simplifies to Eq. (18).

$$I_0(x,y) = a_0[T_w]I_b[T_w], (x,y) \in \partial\mathscr{D}_e \quad (18)$$

with $a_0 = F\left(C_{min}, T_g, T_b\right)$ computed from the ALBDF set in Eq. (6).

Due to the complexity of computations arising from the large number of spectral bands, the Planck-mean absorption coefficient is introduced by modifying Eq. (16) into Eq. (19).

$$\sin\theta\cos\varphi\frac{\partial I(x,y,\theta,\varphi)}{\partial x} + \sin\theta\sin\varphi\frac{\partial I(x,y,\theta,\varphi)}{\partial y} = \kappa_p[I_b[T(x,y)] - I(x,y,\theta,\varphi)], \quad (19)$$

subjected to boundary conditions given by Eq. (20):

$$I(x,y,\theta,\varphi) = I_b[T_w], (x,y) \in \partial\mathscr{D}_e, (\theta,\varphi) \in \Theta^\Omega. \quad (20)$$

The radiative integral solutions based on Eq. (19) for a gray medium have been previously evaluated using the semi-analytical and ray-tracing methods, as documented in Refs. [20,21,32].

4.4.1. Radiative integral solutions of RTE combined with SLW correlated method

Discrete absorption coefficients and associated weights $\left(k_g, a_g\right)$ are computed for various constant values of temperatures T_g, with negligible temperature difference observed at the boundaries (T_w). In fact, the weighted absorption coefficients exhibit only minor variations with temperature of the medium $T(x,y)$. Consequently, by solving Eq. (16), the exact integral solution for non-isothermal gas flow is obtained. It gives the parameterized incoming radiation $I_g(x,y,\theta,\varphi)$ for each discrete gray gas ($g = 1,2\ldots N_g$) as specified in Eq. (21).

$$I_g(x,y,\theta,\varphi) = I_{gw}(x,y)e^{-k_g\delta(x,y,\theta,\varphi)} + k_g\int_0^{\delta(x,y,\theta,\varphi)} I_{b_g}[T(x',y')]e^{-k_g\delta'}d\delta', \quad (21)$$

where δ and δ' represent the curvilinear abscissa of the ray pathway in the medium, $x' \in [0,x]$ and $y' \in [0,y]$. The weighted radiation intensity that leaves each wall I_{gw} is given following Eq. (22):

$$I_{gw} = a_g[T_w]I_b[T_w], (x,y) \in \partial\mathscr{D}_e\ . \quad (22)$$

The weighted coefficients a_g, associated with the wall temperature T_w are determined in accordance with Eq. (23):

$$a_{gw} = F\left(\tilde{C}_g^{ref}, T_g = T(x,y), T_b = T_w\right) - F\left(\tilde{C}_{g-1}^{ref}, T_g = T(x,y), T_b = T_w\right). \quad (23)$$

If the participating gas is in an isothermal state, $T(x',y') = T(x,y) = c$, $c \in \mathbb{R}$. Then, Eq. (21) transforms into Eq. (24):

$$I_g(x,y,\theta,\varphi) = I_{gw}(x,y)e^{-k_g\delta(x,y,\theta,\varphi)} + \left(1 - e^{-k_g\delta(x,y,\theta,\varphi)}\right)I_{b_g}. \quad (24)$$

4.4.2. Incident radiation

The incident radiation of each discrete gray gas within the rectangular geometry is computed along $\vec{\Omega}$, for the North, East, South, and West walls, denoted by G_g^N, G_g^E, G_g^S and G_g^W, respectively. The radiation intensity of a discrete gray gas at any point $M(x,y) \in \{\mathscr{D}\}$, encompassing all directions of $\vec{\Omega}$, is evaluated using Eqs. (25a, 25b):

$$G_g(x,y) = 2\int_{\theta=0}^{\theta=\pi}\int_{\varphi=0}^{\varphi=2\pi} I_g(x,y,\theta,\varphi)\sin\theta d\theta d\varphi \quad (25a)$$

$$G(x,y) = \sum_{g=0}^{N_g} G_g(x,y)\ . \quad (25b)$$

An analogous procedure to that described in Refs. [20,21] was followed to evaluate the exact semi-analytical expressions of the incident radiation. It has been expressed in terms of the first- and second-order Bickley-Naylor functions, Ki_1, Ki_2 respectively. So, let us define the nth-order Bickley-Naylor functions, Ki_n as in Eq. (26):

$$Ki_n(u) = \int_{\theta=0}^{\theta=\frac{\pi}{2}} e^{-\frac{u}{\sin\theta}}(\sin\theta)^{n-1}d\theta, n \in \mathbb{N}, u \in \mathbb{R}^+, \quad (26)$$

with, $Ki_{2n}(0) = \frac{2^{2(n-1)}(n-1)!}{(2n-1)!}$ and $Ki_{2n+1}(0) = \frac{\pi(2n-1)!}{2^{2n}n!}$. The radiative integrals associated with the involved gas species are calculated and expressed using these specific functions. These functions result from Laplace transformations and are classified as generalised exponential integral functions; they cannot be evaluated analytically. For any positive integer $n \in \mathbb{N}$, all the Ki_n functions are monotonously decreasing, since the function $e^{-\frac{u}{\sin\theta}}$ decreases, $(\sin\theta)^{n-1}$ increases and is positive.

Bickley-Naylor functions Ki_n are also described following series expansions. Then, the series expansion of the first and second order Bickley-Naylor functions Ki_1, Ki_2 are given in Appendix. B. If, $u \gg 1$, an asymptotic expansion is applied and given by Eq. (27):

$$Ki_n(u) \approx \sqrt{\frac{\pi}{2u}} e^{-u} \left\{ 1 - \frac{(4n+1)}{8u} + \frac{3(6n^2+24n+3)}{2!(8u)^2} - \ldots \right\}, n \in \mathbb{N}. \quad (27)$$

Indeed, the respective discretised integral solutions for the incident radiation within the two-dimensional rectangular geometry are obtained after solving the RTE. The expected radiative quantities are then expressed using their dimensionless formulation, as defined in Appendix. C. Following the rays' directions from the East wall (Γ_E) to any calculation point $M(x,y) \in \{\mathscr{D}\}$, the dimensionless incident radiation is given by Eq. (28):

$$G_g^*\left(x_i,y_j\right)\Big|_E = \frac{a_{gE}T_E^4}{4T_{hot}^4}\left\{\varphi_{E_1}^{ij}\sum_{l=1}^{N_\varphi}\omega_l Ki_2\left(\frac{k_g(H_x-x_i)}{cos\,\varphi_{l_1}}\right)+\varphi_{E_2}^{i,j} \times \sum_{l=1}^{N_\varphi}\omega_l Ki_2\left(\frac{k_g(H_x-x_i)}{cos\,\varphi_{l_2}}\right)\right\}$$

$$+a_g k_g(H_x-x_i)\varphi_{E_1}^{i,j}\sum_{l=1}^{N_\varphi}\sum_{m=1}^{M}\frac{\omega_m\omega_l}{cos\,\varphi_{l_1}}\frac{T^4\left(x_i',y_j'\right)}{4T_{hot}^4}Ki_1\left(\frac{k_g(H_x-x_i)\delta_m}{cos\,\varphi_{l_1}}\right)$$

$$+a_g k_g(H_x-x_i)\varphi_{E_2}^{i,j}\sum_{l=1}^{N_\varphi}\sum_{m=1}^{M}\frac{\omega_m\omega_l}{cos\,\varphi_{l_2}}\frac{T^4\left(x_i',y_j'\right)}{4T_{hot}^4}Ki_1\left(\frac{k_g(H_x-x_i)\delta_m}{cos\,\varphi_{l_2}}\right), \quad (28)$$

where, $\varphi_{E_1}^{i,j} = tan^{-1}\left\{\frac{H_y-y_j}{H_x-x_i}\right\}$, $\varphi_{E_2}^{i,j} = tan^{-1}\left\{\frac{y_j}{H_x-x_i}\right\}$, $\varphi_{l_1} = \delta_l \times \varphi_{E_1}^{i,j}$, $\varphi_{l_2} = \delta_l \times \varphi_{E_2}^{i,j}$.

In the direction from the North wall (Γ_N) to the point $M(x,y) \in \{\mathscr{D}\}$, the dimensionless incident radiation is given by Eq. (29):

$$G_g^*\left(x_i,y_j\right)\Big|_N = \frac{a_{gN}T_N^4}{4T_{hot}^4}\left\{\varphi_{N_1}^{i,j}\sum_{l=1}^{N_\varphi}\omega_l Ki_2\left(\frac{k_g\left(H_y-y_j\right)}{cos\,\varphi_{l_3}}\right)+\varphi_{N_2}^{i,j} \times \sum_{l=1}^{N_\varphi}\omega_l Ki_2\left(\frac{k_g\left(H_y-y_j\right)}{cos\,\varphi_{l_4}}\right)\right\}$$

$$+a_g k_g\left(H_y-y_j\right)\varphi_{N_1}^{i,j}\sum_{l=1}^{N_\varphi}\sum_{m=1}^{M}\frac{\omega_m\omega_l}{cos\,\varphi_{l_3}}\frac{T^4\left(x_i',y_j'\right)}{4T_{hot}^4}K_{i_1}\left(\frac{k_g\left(H_y-y_j\right)\delta_m}{cos\,\varphi_{l_3}}\right)$$

$$+a_g k_g\left(H_y-y_j\right)\varphi_{N_2}^{i,j}\sum_{l=1}^{N_\varphi}\sum_{m=1}^{M}\frac{\omega_m\omega_l}{cos\,\varphi_{l_4}}\frac{T^4\left(x_i',y_j'\right)}{4T_{hot}^4}K_{i_1}\left(\frac{k_g\left(H_y-y_j\right)\delta_m}{cos\,\varphi_{l_4}}\right), \quad (29)$$

where, $\varphi_{N_1}^{i,j} = tan^{-1}\left\{\frac{H_x-x_i}{H_y-y_j}\right\}$, $\varphi_{N_2}^{i,j} = tan^{-1}\left\{\frac{x_i}{H_y-y_j}\right\}$, $\varphi_{l_3} = \delta_l \times \varphi_{N_1}^{i,j}$ and $\varphi_{l_4} = \delta_l \times \varphi_{N_2}^{i,j}$.

The directions from the West (Γ_W) and South (Γ_S) walls to the point $M(x,y) \in \{\mathscr{D}\}$ are given by: $G_g^*\left(x_i,y_j\right)\Big|_W = G_g^*\left(H_x-x_i,y_j\right)\Big|_E$ and $G_g^*\left(x_i,y_j\right)\Big|_S = G_g^*\left(x_i,H_y-y_j\right)\Big|_N$.

The dimensionless incident radiation in the directions of $\overrightarrow{\Omega}$ for each gas species is determined by the relation given in Eq. (30):

$$G_g^*\left(x_i,y_j\right)\Big|_{\{\mathscr{D}\}} = G_g^*\left(x_i,y_j\right)\Big|_E + G_g^*\left(x_i,y_j\right)\Big|_N + G_g^*\left(x_i,y_j\right)\Big|_W + G_g^*\left(x_i,y_j\right)\Big|_S. \quad (30)$$

The resulting dimensionless radiative intensity of non-gray gases is the sum of the contributions from the discrete gray gases in the medium. It is calculated using Eq. (30), and is expressed by Eq. (31) as:

$$G^*\left(x_i,y_j\right) = \sum_{g=0}^{N_g} G_g^*\left(x_i,y_j\right), \forall\left(x_i,y_j\right) \in \{\mathscr{D}\} \quad (31)$$

4.4.3. Radiative flux and source term

The radiative flux vector of non-gray gases, discretised as gray gases, is defined below by Eq. (32):

$$\overrightarrow{q}^r(x,y) = 2\sum_{g=0}^{N_g}\int_{\varphi=0}^{\varphi=2\pi}\int_{\theta=0}^{\theta=\pi} I_g(x,y,\theta,\varphi)(sin\,\theta)^2\begin{pmatrix} cos\,\varphi \\ sin\,\varphi \end{pmatrix} d\theta d\varphi \quad (32)$$

The radiative source $S^r = -\overrightarrow{\nabla}.\overrightarrow{q}^r(x,y)$, decreases in the direction opposite to the flux divergence and is given by Eq. (33) as:

$$\overrightarrow{\nabla}.\overrightarrow{q}^r(x,y) = \sum_{g=0}^{N_g} k_g\left[4\pi a_g I_b[T(x,y)] - G_g(x,y)\right], \quad (33)$$

with the dimensionless radiative source term given by Eq. (33) and Eq. (34a),

$$S^{r*} = \sum_{g=0}^{N_g} k_g\left[G_g^* - a_g T^{*4}\right], \quad (34a)$$

where, $T^{*4} = T^4/T_{hot}^4$. When considering the Planck-mean absorption coefficient κ_p as part of the evaluation of a radiative source in Eq. (34a), its formulation changes and becomes as shown in Eq. (34b):

$$S^{r*} = \kappa_p\left[G^* - T^{*4}\right]. \quad (34b)$$

Exact semi-analytical expressions for the radiative heat flux are derived following calculations based on Eq. (33). The use of second and third-order specific functions Ki_2 and Ki_3 removes the integral dependence on the variables θ and φ as elaborated in Refs. [20,21]. The resulting radiative heat flux vector for each discrete gray gas follows the direction $\overrightarrow{\Omega}$.

For the direction extending from the East wall (Γ_E) to any calculation point $M(x,y) \in \{\mathscr{D}\}$, the dimensionless radiative heat flux vector is given by Eq. (35):

$$\overrightarrow{q}_g^*\left(x_i,y_j\right)\Big|_E = \frac{a_{gE}T_E^4}{4T_{hot}^4}\begin{pmatrix} \varphi_{E_1}^{ij}\sum_{l=1}^{N_\varphi}\omega_l Ki_3\left(\frac{k_g(H_x-x_i)}{cos\,\varphi_{l_1}}\right)cos\,\varphi_{l_1} + \varphi_{E_2}^{i,j}\sum_{l=1}^{N_\varphi}\omega_l Ki_3\left(\frac{k_g(H_x-x_i)}{cos\,\varphi_{l_2}}\right)cos\,\varphi_{l_2} \\ \varphi_{E_1}^{ij}\sum_{l=1}^{N_\varphi}\omega_l Ki_3\left(\frac{k_g(H_x-x_i)}{cos\,\varphi_{l_1}}\right)sin\,\varphi_{l_1} - \varphi_{E_2}^{i,j}\sum_{l=1}^{N_\varphi}\omega_l Ki_3\left(\frac{k_g(H_x-x_i)}{cos\,\varphi_{l_2}}\right)sin\,\varphi_{l_2} \end{pmatrix}$$

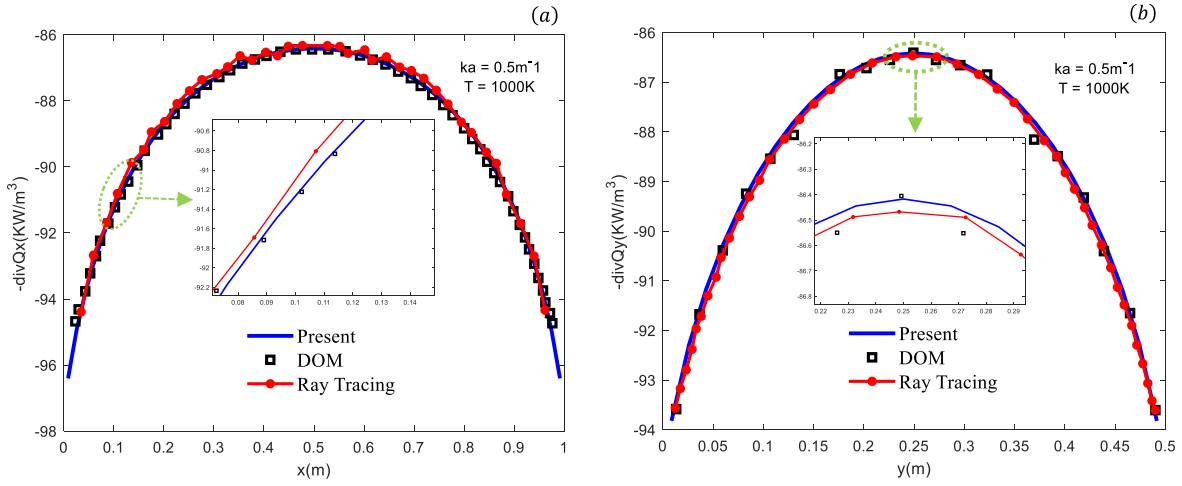

Fig. 2. Radiative source term along the centerlines of the rectangular geometry: (a) at $y = \frac{H_y}{2}$, (b) at $x = \frac{H_x}{2}$.

$$+a_g k_g (H_x - x_i)\varphi_{E_1}^{i,j} \times \sum_{l=1}^{N_\varphi}\sum_{m=1}^{M} \frac{\omega_m \omega_l}{\cos\varphi_{l_1}} \frac{T^4\left(x_i', y_j'\right)}{4T_{hot}^4} Ki_2\left(\frac{k_g(H_x - x_i)\delta_m}{\cos\varphi_{l_1}}\right)\begin{pmatrix}\cos\varphi_{l_1}\\ \sin\varphi_{l_1}\end{pmatrix}$$

$$+a_g k_g (H_x - x_i)\varphi_{E_2}^{i,j} \times \sum_{l=1}^{N_\varphi}\sum_{m=1}^{M} \frac{\omega_m \omega_l}{\cos\varphi_{l_2}} \frac{T^4\left(x_i', y_j'\right)}{4T_{hot}^4} Ki_2\left(\frac{k_g(H_x - x_i)\delta_m}{\cos\varphi_{l_2}}\right)\begin{pmatrix}\cos\varphi_{l_2}\\ -\sin\varphi_{l_2}\end{pmatrix}. \quad (35)$$

Along the direction from the North wall (Γ_N) to the point $M(x,y) \in \{\mathscr{D}\}$, the dimensionless radiative heat flux vector is expressed as in Eq. (36):

$$\left.\overrightarrow{q}_g^{\,*}\left(x_i, y_j\right)\right|_N = \frac{a_{gN} T_N^4}{4T_{hot}^4} \begin{pmatrix} \varphi_{N_1}^{i,j} \sum_{l=1}^{N_\varphi} \omega_l Ki_3\left(\frac{k_g\left(H_y - y_j\right)}{\cos\varphi_{l_3}}\right)\sin\varphi_{l_3} - \varphi_{N_2}^{i,j} \sum_{l=1}^{N_\varphi} \omega_l Ki_3\left(\frac{k_g\left(H_y - y_j\right)}{\cos\varphi_{l_4}}\right)\sin\varphi_{l_4} \\ \varphi_{N_1}^{i,j} \sum_{l=1}^{N_\varphi} \omega_l Ki_3\left(\frac{k_g\left(H_y - y_j\right)}{\cos\varphi_{l_3}}\right)\cos\varphi_{l_3} + \varphi_{N_2}^{i,j} \sum_{l=1}^{N_\varphi} \omega_l Ki_3\left(\frac{k_g\left(H_y - y_j\right)}{\cos\varphi_{l_4}}\right)\cos\varphi_{l_4} \end{pmatrix}$$

$$+a_g k_g \left(H_y - y_j\right)\varphi_{N_1}^{i,j} \times \sum_{l=1}^{N_\varphi}\sum_{m=1}^{M} \frac{\omega_m \omega_l}{\cos\varphi_{l_3}} \frac{T^4\left(x_i', y_j'\right)}{4T_{hot}^4} Ki_2\left(\frac{k_g\left(H_y - y_j\right)\delta_m}{\cos\varphi_{l_3}}\right)\begin{pmatrix}\sin\varphi_{l_3}\\ \cos\varphi_{l_3}\end{pmatrix}$$

$$+a_g k_g \left(H_y - y_j\right)\varphi_{N_2}^{i,j} \times \sum_{l=1}^{N_\varphi}\sum_{m=1}^{M} \frac{\omega_m \omega_l}{\cos\varphi_{l_4}} \frac{T^4\left(x_i', y_j'\right)}{4T_{hot}^4} Ki_2\left(\frac{k_g\left(H_y - y_j\right)\delta_m}{\cos\varphi_{l_4}}\right)\begin{pmatrix}-\sin\varphi_{l_4}\\ \cos\varphi_{l_4}\end{pmatrix}. \quad (36)$$

Along the directions covering the West (Γ_W) and South (Γ_S) walls, the following relation is obtained, $\left.\overrightarrow{q}_g^{\,*}\left(x_i, y_j\right)\right|_W = \left.\overrightarrow{q}_g^{\,*}\left(H_x - x_i, y_j\right)\right|_E$ and $\left.\overrightarrow{q}_g^{\,*}\left(x_i, y_j\right)\right|_S = \left.\overrightarrow{q}_g^{\,*}\left(x_i, H_y - y_j\right)\right|_N$.

The resulting dimensionless radiative heat flux of gases burning in the furnace is therefore deducted and given with Eq. (37):

$$\left.\overrightarrow{q}^{r^*}\left(x_i, y_j\right)\right|_{\{\mathscr{D}\}} = \sum_{g=0}^{N_g} \left\{ \left.\overrightarrow{q}_g^{\,*}\left(x_i, y_j\right)\right|_E + \left.\overrightarrow{q}_g^{\,*}\left(x_i, y_j\right)\right|_N + \left.\overrightarrow{q}_g^{\,*}\left(x_i, y_j\right)\right|_W + \left.\overrightarrow{q}_g^{\,*}\left(x_i, y_j\right)\right|_S \right\} \quad (37)$$

Therefore, the numerical solutions of the radiative integrals presented above are examined and interpreted in the next section.

5. Validation, numerical results and discussion

This section presents and discusses the integral solutions of the RTE combined with the radiative properties of gases, obtained using the SLW correlated model and the ray-tracing method. The numerical results are presented for CO_2 /N_2, H_2O/N_2 and mixed CO_2 /H_2O/N_2 gases burning in a two-dimensional geometry. The gas radiative source term, temperature distribution, and radiative heat flux profiles are determined as part of the radiative analysis. Furthermore, suitable numerical simulations of the temperature distribution and radiative heat flux have been conducted, to gain deeper insight into the heat-transfer contours. Computations have been performed with a computer DESKTOP, Intel(R) Core (TM) i7-6700HQ CPU@ 2.60 GHz 2.59 GHz, using FORTRAN95 software.

5.1. Computation

The algorithms used in this study proceed through several computational steps, summarized as follows.

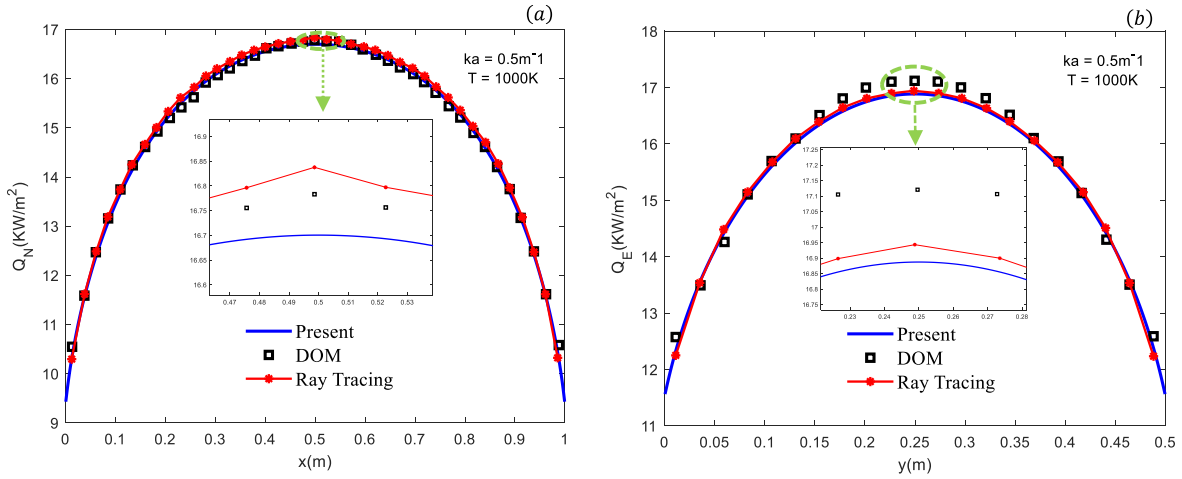

Fig. 3. Radiative flux at walls of the rectangular geometry: (a) North wall, (b) East wall.

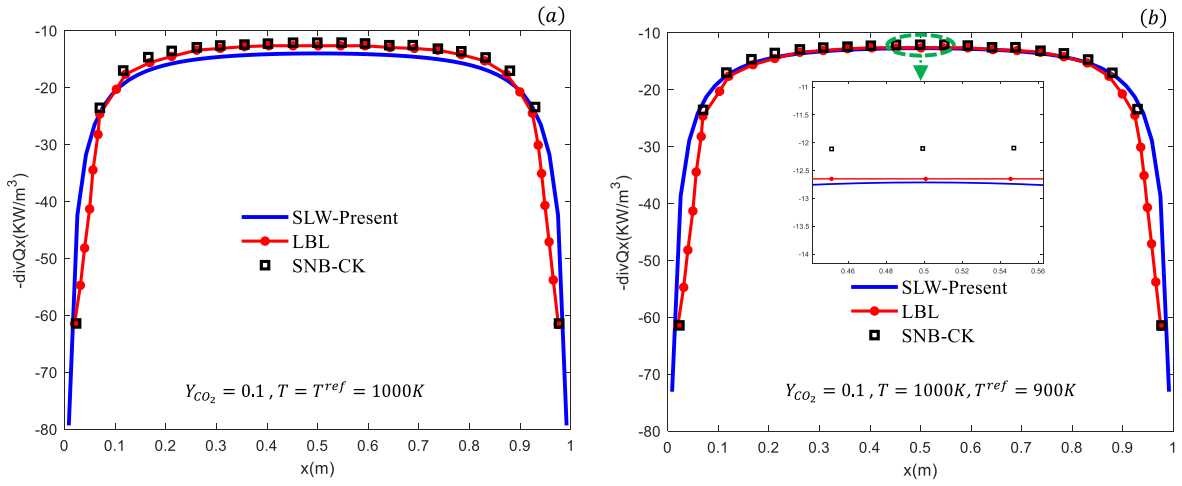

Fig. 4. Radiative source term of CO_2/N_2 along the centerline $y = \frac{H_y}{2}$ inside the rectangular geometry: (a) $T = T^{ref} = 1000K$, (b) $T = 1000K$, $T^{ref} = 900K$.

a. Initialise the total number of discrete gray gases N_g, chemical concentrations Y_s, gas temperatures $T_b = T^{loc}$ and $T_g = T^{ref}$, then compute the supplemental absorption cross section $\widetilde{C}_g$ using Eq. (4).
b. Insert the values of $\widetilde{C}_g$ into the SLW-correlated model using the ALBDF from Eq. (3) and Pearson correlated coefficients [18,19], to compute the weighted coefficients a_g and the associated discrete absorption coefficients k_g.
c. Determine the Planck-mean absorption coefficients κ_p from Eq. (11).
d. Using (a_g, k_g) and κ_p with the RTE from Eq. (16) and Eq. (19); compute the radiative heat flux and source terms from Eqs. (34a,

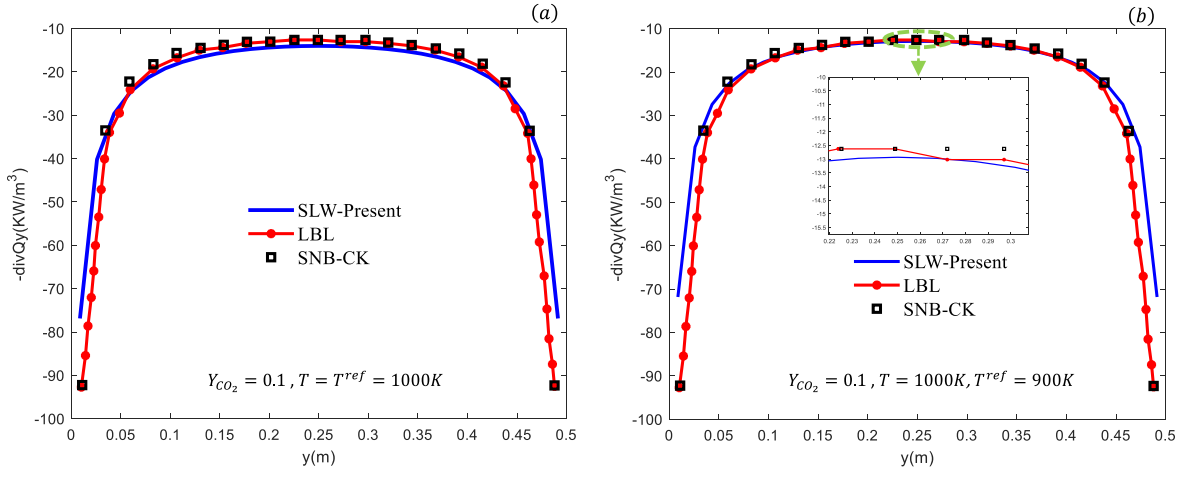

Fig. 5. Radiative source term of CO_2/N_2 along the centerline $x = \frac{H_x}{2}$ inside the rectangular geometry: (a) $T = T^{ref} = 1000K$, (b) $T = 1000K$, $T^{ref} = 900K$.

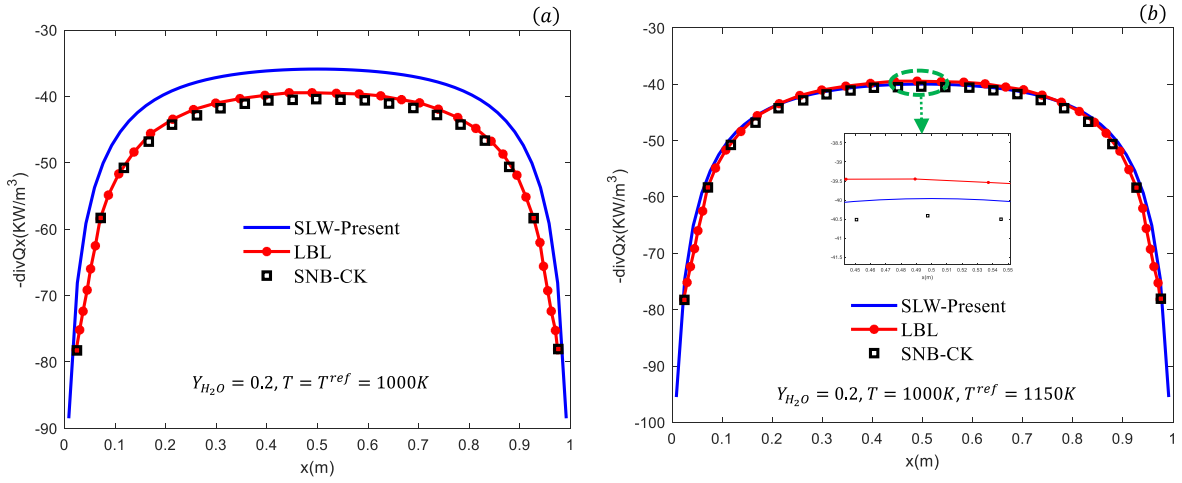

Fig. 6. Radiative source term of H_2O/N_2 along the centerline $y = \frac{H_y}{2}$ inside the rectangular geometry: (a) $T = T^{ref} = 1000K$, (b) $T = 1000K$, $T^{ref} = 1150K$.

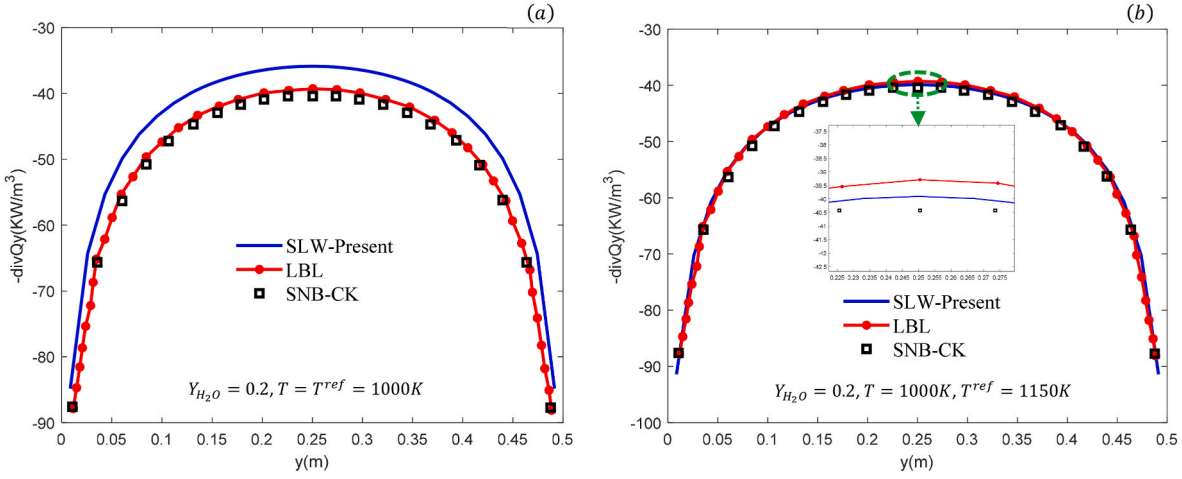

Fig. 7. Radiative source term of H_2O/N_2 along the centerline $x = \frac{H_x}{2}$ inside the rectangular geometry: (a) $T = T^{ref} = 1000K$, (b) $T = 1000K$, $T^{ref} = 1150K$.

34b) at a prescribed temperature; determine the dimensionless radiation intensity G^* from Eq. (21) at radiative equilibrium via an iterative scheme.

e. Compute the temperature distribution T^* at radiative equilibrium, iterating until the convergence criterion $Max\left[\frac{(T^*)_{ij}^{n+1}-(T^*)_{ij}^{n}}{(T^*)_{ij}^{n}}\right] \leq 10^{-5}$ is satisfied.

Parameters such as the number of discrete gray gases, the quadrature angles for the RTE solver, and the mesh resolution each influence the CPU time and the accuracy of the computed thermal quantities. Although calculations of S^{r^*}, G^*, and T^* with (a_g, k_g) from Eq. (16), require more computational time and resources, they yield more accurate results than using κ_p from Eq. (19).

5.2. Validation

5.2.1. Thermal radiation with one discrete gray gas

The aim is to validate the accuracy of RTE's solver, which was developed using the ray-tracing method, and to ensure that it does not affect the performance of the designed non-gray gas model. Calculations have been performed for a homogeneous, semi-transparent rectangular medium filled with a unit gray gas, as illustrated in Fig. 1(a and b). The walls are assumed to be black and cold, while the temperature of the medium is maintained at $1000K$ with a constant gray absorption coefficient of $k_a = 0.5m^{-1}$, as analysed by Chu et al. [8]. The computations were carried out for a rectangular enclosure of dimensions $H_x \times H_y = 1.0m \times 0.5m$, with $H_y = \frac{H_x}{2}$ discretised using a 61×31 mesh grid. To verify the accuracy of the present RTE solver, the radiation source terms and radiative flux component profiles along the enclosure centerline are computed. The results have been compared with those obtained using the DOM and ray-tracing methods reported by Goutiere et al. [6] and Chu et al. [8]. Accordingly, Fig. 2(a and b) illustrates the radiative flux profiles along the centerlines of the rectangular enclosure.

The semi-analytical RTE solver exhibits a maximum deviation of under 0.15 % relative to the ray-tracing results of Goutiere et al. [6] and the DOM solutions reported in Ref. [8]. The relevance of the semi-analytical method, supported by numerical simulations, has already been demonstrated in Refs. [20,21] for both simple and complex geometries. Fig. 3(a and b) show the radiative flux profiles along the North ($x \in [0, H_x], y = H_y$) and East ($x = 0, y \in [0, H_y]$) walls. The results demonstrate the accuracy and reliability of the RTE's solver in comparison with those reported by Goutiere et al. [6] and Chu et al. [8].

The semi-analytical method used with specific functions, yields a discrepancy of less than 0.1 % compared with the reference ray-tracing method proposed in Ref. [6] and less than 0.3 % relative to the DOM results reported in Ref. [8].

Table 1
Net radiative flux values and relative errors at the center and right walls, and radiative source term at the center of the rectangular geometry.

Y_s, $T_g = T_b(K)$	$10\%CO_2/N_2$ at $1000K$			$20\%H_2O/N_2$ at $1000K$		
q, $-\nabla q$	$q(KW/m^2)$		$-\nabla q(KW/m^3)$	$q(KW/m^2)$		$-\nabla q(KW/m^3)$
(x,y)	$(1m, 0.25m)$	$(0.5m, 0.5m)$	$(0.5m, 0.25m)$	$(1m, 0.25m)$	$(0.5m, 0.5m)$	$(0.5m, 0.25m)$
LBL [31]	5.544	5.591	− 12.902	10.376	10.481	− 39.522
SNB-CK [31]	5.372	5.417	− 12.470	10.521	10.624	− 40.418
SLW-Present	5.406	5.575	− 12.929	10.322	10.480	− 39.906
|LBL − SLW|/ LBL	0.024	0.002	− 0.002	0.005	0.0001	− 0.009

Table 2
Planck-mean absorption coefficients for carbon dioxide, water vapor and their mixture computed at $T_g = T_b = \{500K, 1000K, 3000K\}$.

		$10\%CO_2/N_2$	$20\%H_2O/N_2$	$10\%CO_2/N_2 + 20\%H_2O/N_2$
$T_g = T_b(K)$	N_g	$\kappa_p(m^{-1})$	$\kappa_p(m^{-1})$	$\kappa_p(m^{-1})$
500	5	5.787	4.935	10.722
	10	4.715	3.787	8.502
	20	4.461	3.530	7.991
1000	5	6.855	1.489	8.344
	10	6.095	1.142	7.237
	20	5.893	1.065	6.958
3000	5	0.945	0.100	1.045
	10	0.907	0.077	0.984
	20	0.895	0.072	0.967

5.2.2. *Thermal radiation with non-gray gases*

To validate the combined problem involving radiative transfer (using the ray-tracing method) and the kinetics of non-gray gases from the SLW correlated model, the radiative fluxes and source terms are evaluated. Using the same rectangular geometry illustrated in Fig. 1(a and b), the conditions for Cases 1 and 2, previously studied by Chu et al. [8], have been successfully validated.

Indeed, the boundary surfaces remain black and cold, while the medium maintains a uniform unit total pressure. Fig. 4(a and b) and Fig. 5(a and b) illustrate the radiative source terms of $CO_2/\ N_2$ gases along the x- and y-directions respectively, inside the rectangular enclosure. A total of $N_g = 20$ discrete gray gases are considered, each with a kinetic concentration of $Y_s = 0.1$. The Line-by Line model based on HITEMP 2010 serves as a reference to compare and validate the present results. Calculating radiative quantities with the LBL model is computationally intensive, demanding substantial CPU time and memory, with resource requirements growing for more complex geometries.

For a one-dimensional RTE problem, computation takes over 150 h. The SNB-CK model yields a small relative error and is faster than the LBL model. Computation with the SNB-CK model requires approximately 10 s of CPU time.The proposed correlated SLW model agrees closely with LBL [8] and SNB-CK [8], exhibiting discrepancies below 0.1 % for $x \in [0.1, 0.9]m$ at $T = 1000K$ and $T^{ref} = 900K$.

The discrepancy is less than 2 % for $x \in [0.1, 0.9]m$ at $T = T^{ref} = 1000K$. The discrepancies in the proposed results are more pronounced in the intervals $x \in [0.0, 0.1]m$ and $[0.9, 1]m$ in Fig. 4(a and b), $y \in [0.0, 0.05]m$ and $[0.45, 0.5]m$ in Fig. 5(a and b). As the SLW model is recommended for engineering applications, the correlated SLW model using a reference temperature T^{ref} offers a modest improvement in thermal prediction accuracy. Fig. 6(a and b) and Fig. 7(a and b) show the radiative source term of H_20/N_2 gases along the x- and y-axis respectively, in the 2D geometry for $N_g = 20$ discrete gray gases, $Y_s = 0.2$, $T = 1000K$, and $T^{ref} = 1150K$.

The present SLW-correlated model at $T = T^{ref} = 1000K$, shown in Fig. 7-(a), exhibits a minor discrepancy of less than 3 % compared with the reference LBL [8] and SNB-CK [8] models. Additionally, when a reference temperature for the gases is considered, as shown in Fig. 7-(b), the SLW-correlated model produces more accurate results, reducing the discrepancy to less than 0.2 %.

The accuracy of the present SLW-correlated model was validated by comparing its results with the reference LBL and SNB-CK models from Ref. [8]. SNB-CK model results are generally accepted as reliable in the absence of LBL data. These models first compute the absorption coefficients of participating gases, which are then used in the RTE. The correlated coefficients (b_{lmn}, c_{lmn}, d_{lmn} and u_{lmn}, v_{lmn}, w_{lmn}) proposed by Pearson et al. [19] to compute the ALBDF and the Gaussian quadrature, bring a slight error on the radiative integrals solutions. Table 1 presents the net radiative flux at the center and right-wall positions, as well as the radiative source term at the center of the rectangular geometry Fig. 1(a

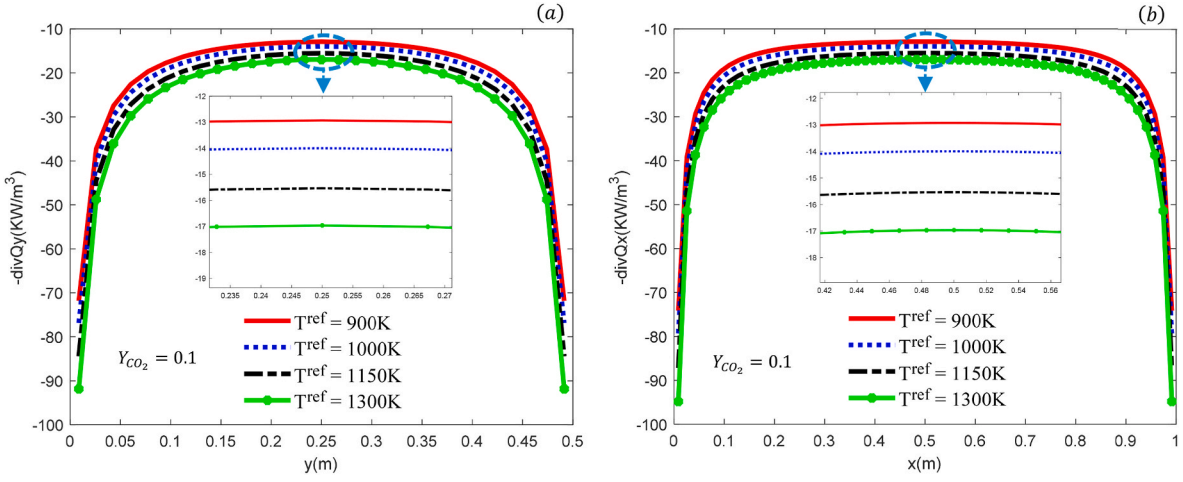

Fig. 8. Radiative source term of CO_2/N_2 along the centerline of a rectangular geometry at $T_g = 1000K$ with a variable reference temperature: (a) at $y = \frac{H_y}{2}$, (b) at $x = \frac{H_x}{2}$.

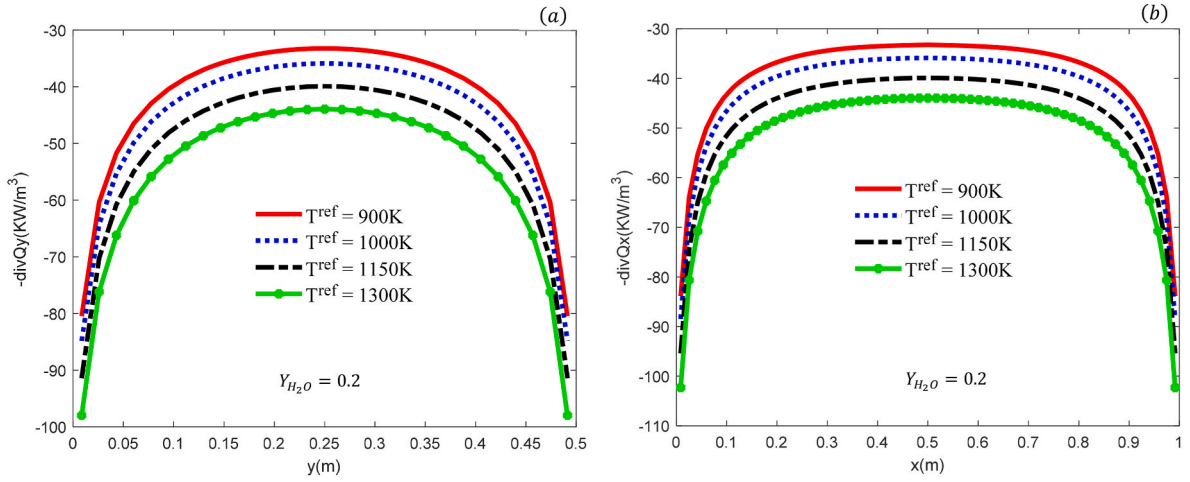

Fig. 9. Radiative source term of H_2O/N_2 along the centerlines of a rectangular geometry at $T_g = 1000K$ with a variable reference temperature: (a) at $y = \frac{H_y}{2}$, (b) at $x = \frac{H_x}{2}$.

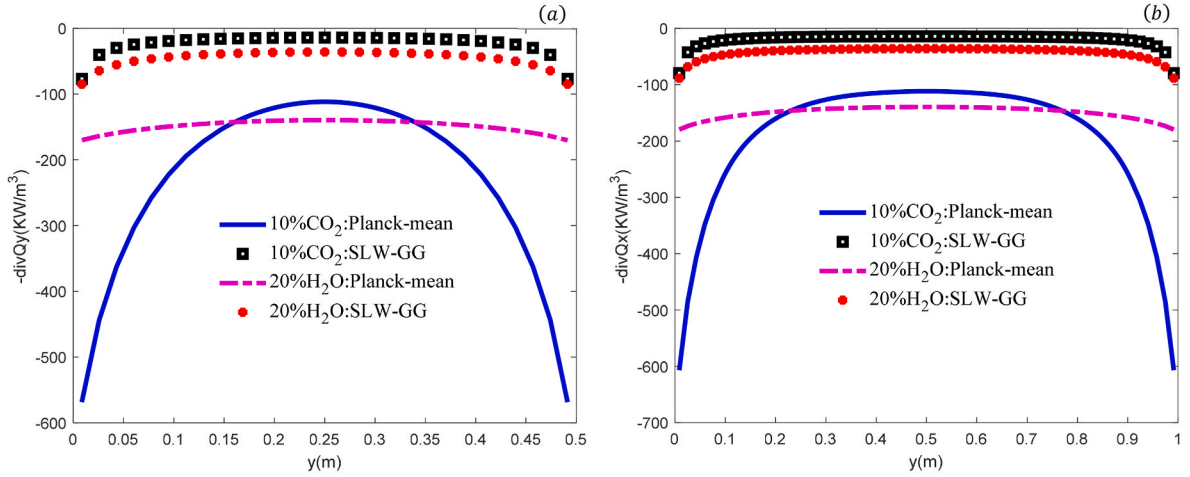

Fig. 10. Radiative source term profiles of $10\%CO_2/N_2$, $20\%H_2O/N_2$ computed with Planck-mean absorption coefficients and discrete absorption coefficients, along the centerline of a the rectangular geometry at $T_g = 1000K$ (a) at $y = \frac{H_y}{2}$, (b) at $x = \frac{H_x}{2}$.

and b). All numerical results were obtained for gases at a uniform temperature of $T = T_g = 1000K$. For both carbon dioxide and water vapor, a reference temperature of $T^{ref} = T_b = 1150K$ was used in the SLW-correlated model. A mean relative error below 3 % relative to the LBL model, for the net radiative heat flux has been obtained. The SLW-correlated model demonstrates higher accuracy for the source term, with errors below 1 %, compared to the SNB-CK model. It yields a relative error up to 4 % for radiative heat flux and source term. Running the algorithms for the above radiation quantities required under 10 s of CPU time.

5.3. Numerical results

5.3.1. Thermal properties of gases: effect of temperature and total discrete number

The spectral evolution of gas radiative properties is used to analyse the distributions of incident radiation, radiative source, temperature, and heat flux in the two-dimensional geometry. Given the known absorption spectral bands of the participating gases [18,28], their Planck-mean absorption coefficients from the SLW-correlated model are presented. Indeed, the radiative properties of CO_2/N_2 and $H_2O/\ N_2$ presented here, enable analysis over the temperature range $300K \leq T_g \leq 4000K$, at a constant pressure of $P = 1\ atm$.

The Planck-mean absorption coefficient κ_p, was also computed for selected representative temperatures. Table 2 displays the computed values for $10\%CO_2/N_2$, $20\%H_2O/N_2$ and their mixture at $T_g = T_b = \{500K, 1000K, 3000K\}$. Thus, accuracy of the SLW-correlated model depends on the number of gray gases, $N_g \in \{5, 10, 20\}$ used to calculate the Planck-mean absorption coefficients. Indeed, when evaluated at $500K$, corresponding to a limited thermal propagation range, the Planck-mean absorption coefficients are higher for both CO_2/N_2 and H_2O/N_2. Thus, upon heat generation, the gases rapidly absorb it, rendering the semi-transparent medium optically thick. At $1000K$, thermal propagation in the medium increases, with carbon dioxide being more refractory to heat and water vapor more transparent. At $3000K$, with increased thermal propagation, both CO_2/N_2 and H_2O/N_2 behave transparently, rendering the semi-transparent medium optically thin. Despite differing gas concentrations, CO_2/N_2 is less transparent to radiative heat transfer than H_2O/N_2 at the same reference temperature during combustion.

5.3.2. Thermal radiation and SLW correlated model

Following validation of the RTE solver with the SLW-correlated gas kinetics equations, this subsection illustrates how selecting an appropriate reference temperature influences the radiative source and inci-

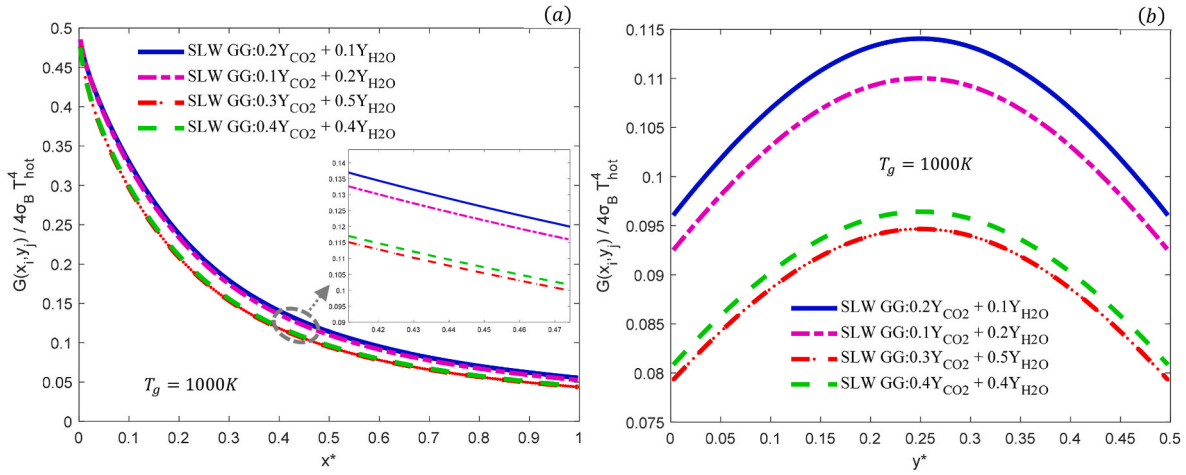

Fig. 11. Dimensionless incident radiation G^* of $CO_2/H_2O/N_2$ mixture along the centerlines of the rectangular geometry for $T_g = T^{ref} = 1000K$ and variable temperature (x,y): (a) at $y = \frac{H_y}{2}$, (b) at $x = \frac{H_x}{2}$.

dent radiation. It also examines the relationship between the SLW discrete gray gas set in Eq. (16) and the Planck-mean absorption coefficients from Eq. (19). The geometrical setup from Sub-section 5.2.1 is retained, with $N_x \times N_y = 61 \times 31$. The gases in the furnace have chemical ratios of $10\%CO_2/N_2$ and $20\%H_2O/N_2$ at $T_g = T = 1000K$, with $N_g = 20$ gray gases and a discrete angular grid of $M_\varphi \times N_\theta = 6 \times 6$.

5.3.2.1. Radiative source: effect of reference temperature. Fig. 8(a and b) and Fig. 9(a and b) present the radiative source profiles of $10\%CO_2/N_2$ and $20\%H_2O/N_2$ along the vertical and horizontal centerlines of the geometry shown in Fig. 1(a and b). Reference temperatures $T^{ref} \in \{900K, 1000K, 1150K, 1300K\}$ were chosen to represent the closest lower and upper values to the gas temperature $T_g = 1000K$, in the participating medium. The radiative source profiles of the participating gases differ due to variations in their absorption spectral bands.

When the reference temperature is below the gas temperature ($T^{ref} < T_g$), the SLW-correlated model slightly overpredicts for both CO_2/N_2 and H_2O/N_2. In contrast, the model underpredicts the radiative source when $T^{ref} > T_g$. The water vapor profiles are more sensitive to variations in the reference temperature compared with carbon dioxide. The same effect of reference temperature can be analysed at radiative equilibrium, even as part of radiative heat flux evaluation. Ultimately, changes in the reference temperature influence the results from both the standard SLW model [25] and the correlated SLW models. This arises from the non-scalable nature of gas absorption spectra across different temperatures in combustion systems.

5.3.2.2. Radiative source: effects of discrete gray gas and Planck-mean. The correlated SLW model enables solving the radiative transfer equation, using either the discrete absorption coefficients k_g and their weights a_g, or directly with the Planck-mean absorption coefficient κ_p. Using either (k_g, a_g) or κ_p in the SLW model leads to different effects in the results. Fig. 10(a and b) shows the radiative source along the centerlines of the rectangular geometry, which clearly demonstrates these effects. For the computations, gas mixtures of $10\%CO_2/N_2$ and $20\%H_2O/N_2$, with $\kappa_p = 5.893\,m^{-1}$ and $\kappa_p = 1.065\,m^{-1}$, at $T_g = T = 1000K$ were used. The reference temperature T^{ref} takes a same value of T_g in this study case.

Analysis of the profiles shows that the curves for carbon dioxide and water vapor gas species exhibit both nonlinearity and symmetry. The parabolic profiles show greater concavity when computed with the Planck-mean absorption coefficients, especially for the optically thick medium ($\kappa_p = 5.893\,m^{-1}$). Solving the RTE with discrete absorption coefficients yields radiative source predictions that are more reliable and less sensitive compared with results using the Planck-mean ab-

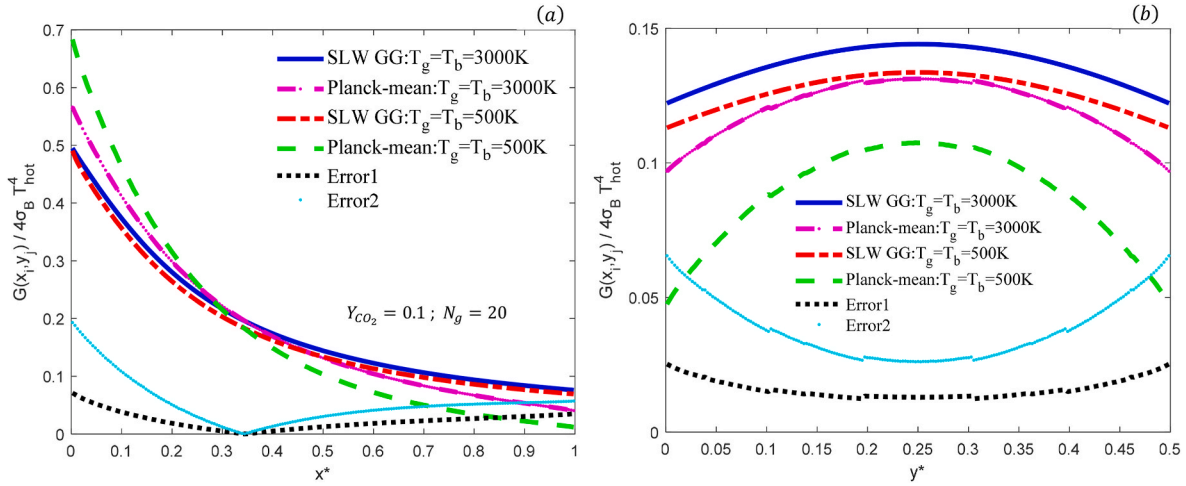

Fig. 12. Incident radiation profiles with Planck-mean absorption coefficients and discrete absorption coefficients along the centerlines of the rectangular geometry for $10\%CO_2/N_2$: (a) $y = \frac{H_y}{2}$, (b) $x = \frac{H_x}{2}$.

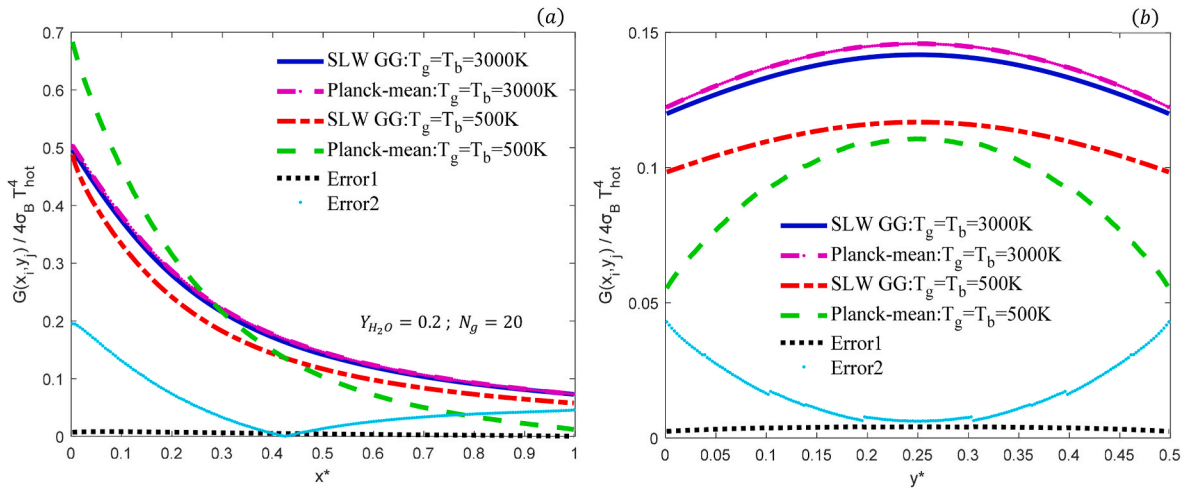

Fig. 13. Incident radiation profiles with Planck-mean absorption coefficients and discrete absorption coefficients along the centerlines of the rectangular geometry for 20%H_2O/N_2: (a) $y = \frac{H_y}{2}$, (b) $x = \frac{H_x}{2}$.

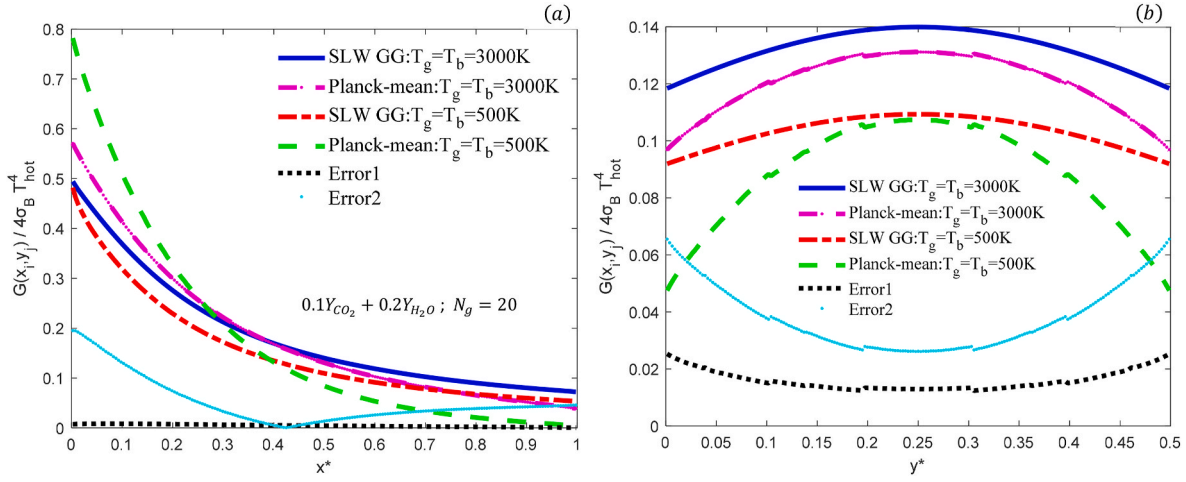

Fig. 14. Incident radiation profiles with Planck-mean absorption coefficients and discrete absorption coefficients along the centerlines of the simple geometry for 10%CO_2/20%H_2O/N_2: (a) $y = \frac{H_y}{2}$, (b) $x = \frac{H_x}{2}$.

Table 3
Computational time of G^* with the Planck-mean κ_p and (k_g, a_g), for carbon dioxide, water vapor and mixtures, for $N_x \times N_y = 251 \times 251$ and $N_g = 20$.

CPU times (s) for $G^* = G(x,y)/4\sigma_B T^4_{hot}$							
		$T_g = 500K$		$T_g = 1000K$		$T_g = 3000K$	
	$M_\varphi \times N_\theta$	κ_p	(k_g, a_g)	κ_p	(k_g, a_g)	κ_p	(k_g, a_g)
10%CO_2/ N_2	4 × 4	54.29 s	2070.48 s	52.01 s	1994.87 s	53.45 s	1999.15 s
	5 × 5	173.18 s	3398.48 s	102.09 s	3065.04 s	103.26 s	3022.65 s
	6 × 6	177.67 s	5230.17 s	174.23 s	4724.79 s	180.25 s	4669.09 s
20%H_2O/ N_2	4 × 4	54.43 s	3131.45 s	56.48 s	2629.35 s	54.63 s	2569.67 s
	5 × 5	102.53 s	3658.04 s	105.78 s	3734.26 s	103.32 s	4520.43 s
	6 × 6	183.56 s	5231.295 s	179.56 s	5279.35 s	174.98 s	5439.81 s
10%CO_2/ N_2	4 × 4	52.56 s	14371.83 s	55.32 s	15765.13 s	52.32 s	17437.19 s
+	5 × 5	108.79 s	22745.20 s	99.64 s	23832.59 s	103.93 s	25091.73 s
20%H_2O/ N_2	6 × 6	172.29 s	31832.57 s	181.92 s	32946.02 s	172.50 s	33473.68 s

sorption coefficients. Comparing the radiative source results from the two approaches at $T_g = 1000K$ yields a mean deviation of $100KW/m^3$.

5.3.2.3. Incident radiation at radiative equilibrium ($S^{r^*} = 0$). At radiative equilibrium, the numerical results follow the assumptions of Sub-section 2. Indeed, the West wall (Γ_W) is hot at T_{hot}, the participating medium starts at T_{hot}, and the remaining walls are cold at $T_0 = T_{cold} = T_{hot}/2$. Radiative integral solutions of the incident radiation $G(x,y)$ are thus computed iteratively until convergence is achieved. Derived from the RTE, $G(x,y)$ is a key thermal quantity for assessing energy transfer in a semi-transparent gas-filled medium. Profiles of the dimensional incident

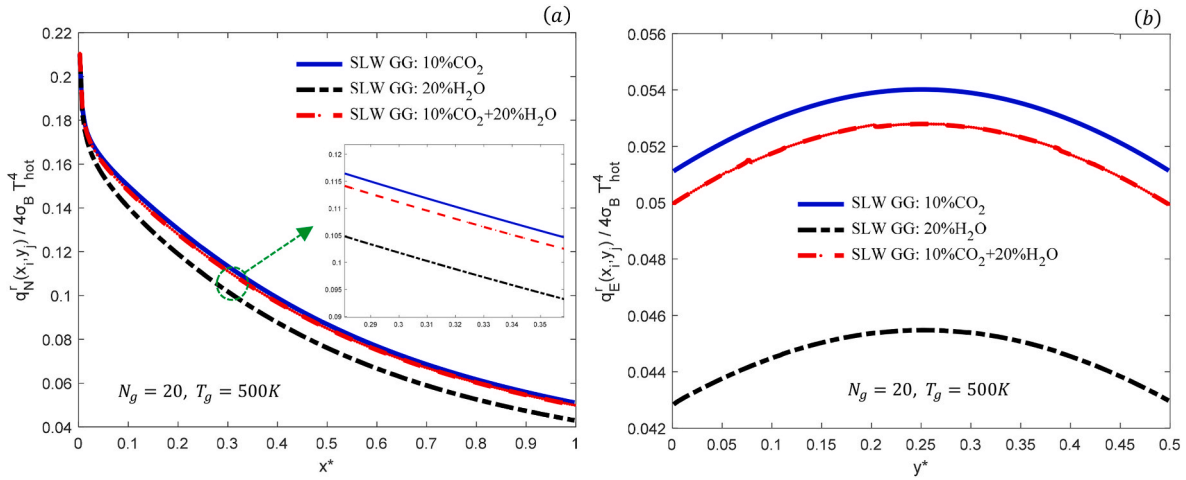

Fig. 15. Radiative heat flux of participating gases $10\%CO_2/N_2$, $20\%H_2O/N_2$ and their mixture for $T_g = 500K$ following: (a) North wall, (b) East wall.

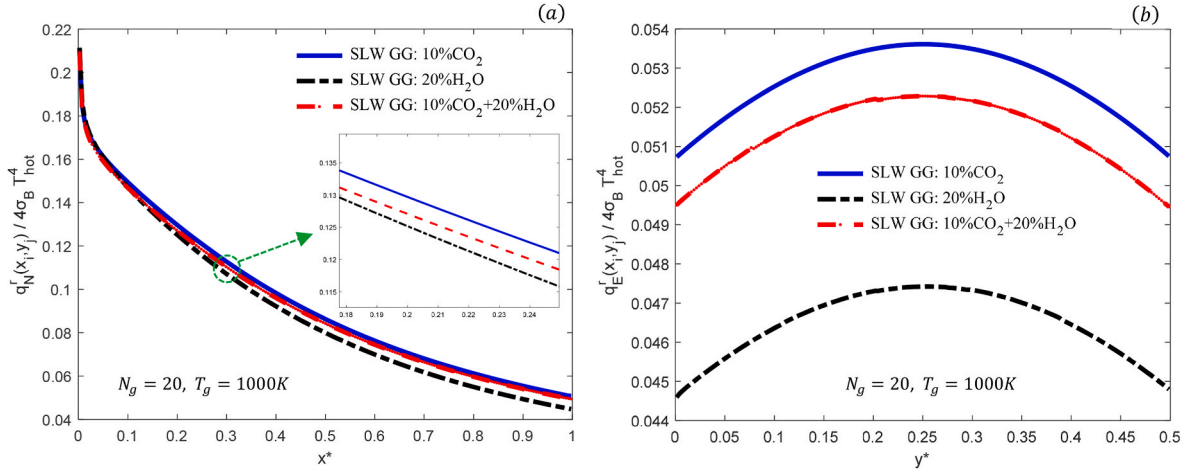

Fig. 16. Radiative heat flux of participating gases $10\%CO_2/N_2$, $20\%H_2O/N_2$ and their mixture for $T_g = 1000K$ following: (a) North wall, (b) East wall.

radiation $G(x,y)/4\sigma_B T_{hot}^4$ for carbon dioxide, water vapor and their mixture, are obtained along the centerlines of the rectangular geometry. Indeed, a mesh grid of $N_x \times N_y = 201 \times 201$ and discrete angles of $M_\varphi \times N_\theta = 6 \times 6$ were used for the computations.

- *Effect of mixture ratios*

Fig. 11-(a) and Fig. 11-(b) highlight the dimensionless incident radiation along the geometry's horizontal and vertical centerlines for the gas mixtures studied. This study aims to assess how each chemical

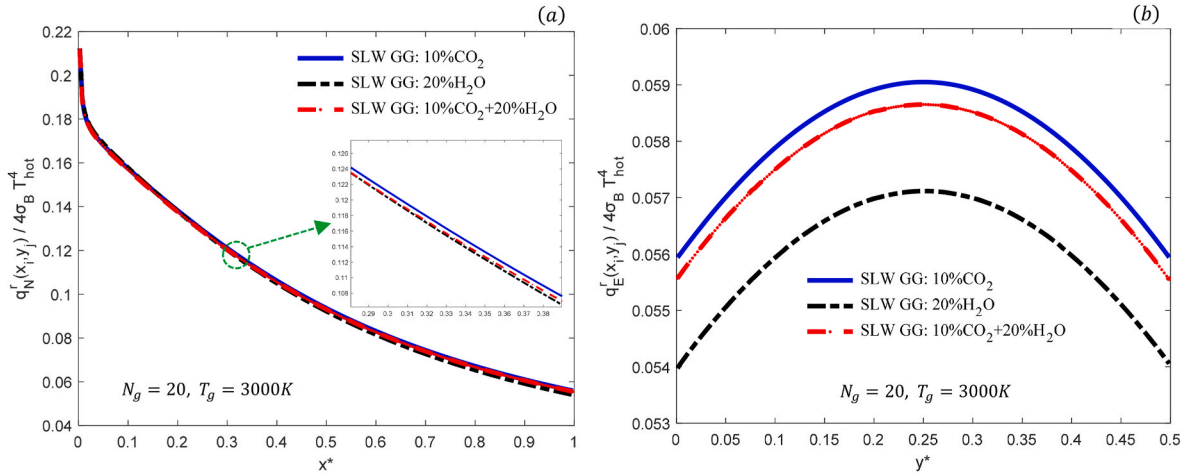

Fig. 17. Radiative heat flux of participating gases $10\%CO_2/N_2$, $20\%H_2O/N_2$ and their mixture for $T_g = 1000K$ following: (a) North wall, (b) East wall.

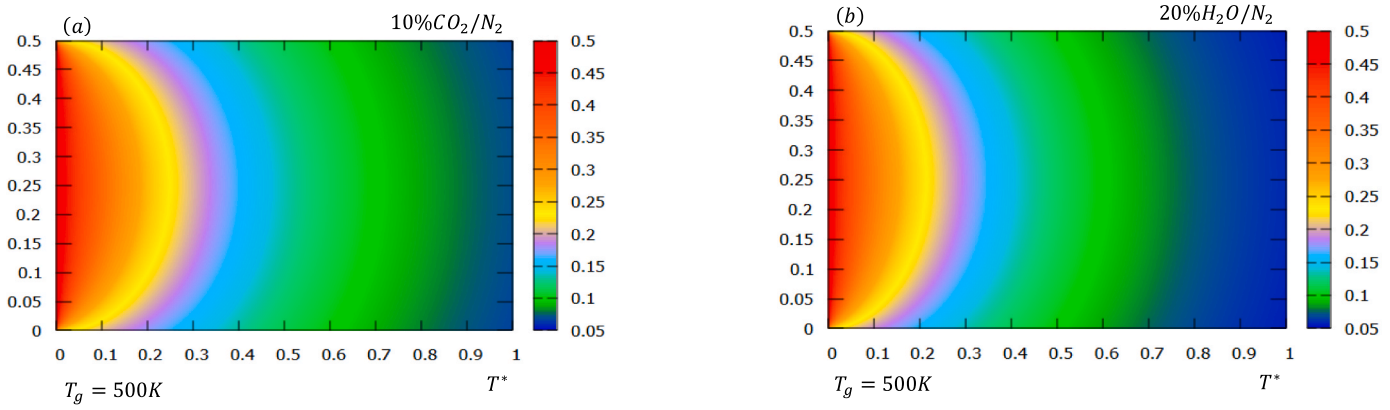

Fig. 18. Dimensionless temperature distribution T^* computed for $T_g = 500K$: (a) $10\%CO_2/N_2$, (b) $20\%H_2O/N_2$.

fraction, Y_{CO_2}, Y_{H_2O} contributes to the overall gas mixture. At $T_g = 1000K$, discrete absorption coefficients and their associated weights (k_g, a_g), the Planck-mean coefficient κ_p were computed and used with the RTE solver following Eq. (16).

Along the horizontal centerline ($y = H_y/2$) in Fig. 11-(a), $G^* \in [0.5, 0.05]$, while in Fig. 11-(b), the profile is symmetric with a peak value of $G^* = 0.14$. Although the G^* profiles for $10\%CO_2 + 20\%H_2O$ and $20\%CO_2 + 10\%H_2O$ have similar shapes, they differ slightly because of variations in the absorption spectral bands of the gases. Nevertheless, the effect persists even though the total chemical ratio is 30 %, with N_2 comprising the remaining 70 %. A similar comparison was made between the G^* profiles for $30\%CO_2 + 50\%H_2O$ and $40\%CO_2 + 40\%H_2O$, where the total chemical ratio is 80 % and N_2 accounts for the remaining 20 %.

- *Effects of discrete gray gas and Planck-mean absorption coefficients*

The plots in Fig. 12(a and b), Fig. 13(a and b) and Fig. 14(a and b) highlight $G^* = G(x,y)/4\sigma_B T_{hot}^4$ along the horizontal and vertical centerlines of the rectangular geometry for the participating gases.

The results obtained with discrete absorption coefficients and Planck-mean absorption coefficients computed at $T_g = 500K$ and $T_g = 3000K$ were subsequently compared. The curves show a decrease in G^* along the horizontal centerline and a parabolic profile along the vertical centerline. The mean deviation plots, $Error1 = \left|G^*_{SLW\ GG} - G^*_{Planck-mean}\right|_{3000K}$ and $Error2 = \left|G^*_{SLW\ GG} - G^*_{Planck-mean}\right|_{500K}$, indicate that G^* results using thermal properties at $T_g = 3000K$ have small errors, while those using properties at $T_g = 500K$ exhibit larger deviations.

Across all case studies, *Error*1 exhibits a more stable profile along the geometry's centerlines than *Error*2. From Eq. (34b) at radiative equilibrium $G^* = T^{*4}$, the observations made for G^* can similarly be applied to the dimensionless temperature T^{*4}.

- *Tabulated data of CPU time for G^* with discrete gray gas and Planck-mean*

CPU times for computing the dimensionless incident-radiation $G^* = G(x,y)/4\sigma_B T_{hot}^4$ for the non-gray gases $10\%CO_2/N_2$, $20\%H_2O/N_2$ and $10\%CO_2/20\%H_2O/N_2$ are summarized in Table 3. Gas temperatures $T_g \in \{500K, 1000K, 3000K\}$ and discrete angles $M_\varphi \times N_\theta \in \{6 \times 6, 5 \times 5, 4 \times 4\}$, representing directions of the solid angle Ω, were used to compute the gases' radiative properties (k_g, a_g, κ_p) and to solve the RTE in the rectangular geometry section. CPU times decrease with fewer angular quadratures. Using the Planck-mean absorption coefficients (κ_p), it drastically reduces computation time compared to discrete coefficients (k_g, a_g). For instance, $M_\varphi \times N_\theta = 6 \times 6$ required 183.565 s for $20\%H_2O/N_2$ mixture at $T_g = 500K$, versus 33473.684 s for a $10\%CO_2/20\%H_2O/N_2$ mixture at $T_g = 3000K$.

Significant computational resources and time are required to obtain G^* when using (k_g, a_g), especially for gas mixtures. Therefore, the maximum mean deviations using (k_g, a_g) and κ_p are below 0.2 at $T_g = 500K$ and 0.025 at $T_g = 3000K$, high-temperature engineering calculations can reliably use Planck-mean absorption coefficients (κ_p).

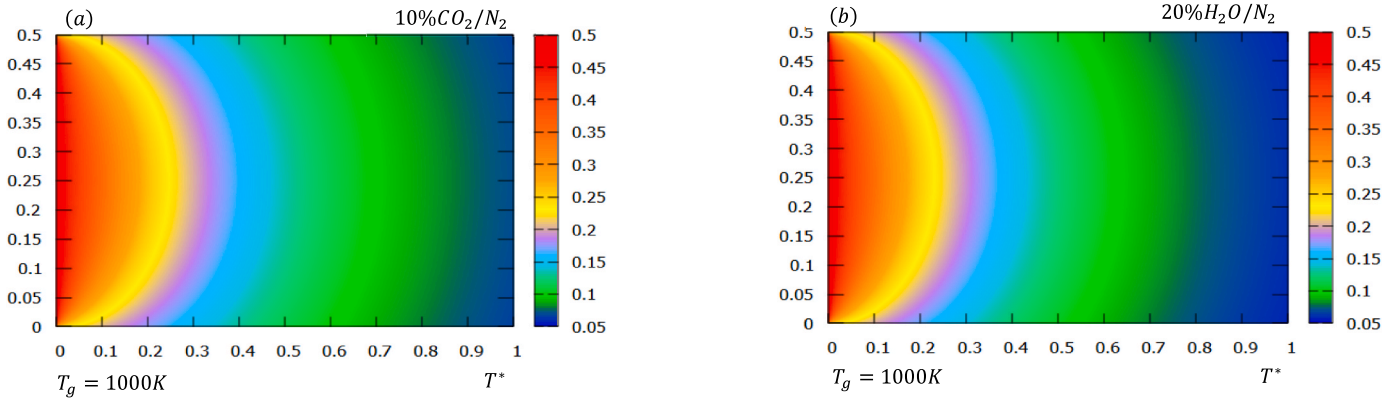

Fig. 19. Dimensionless temperature distribution T^* computed for $T_g = 1000K$: (a) $10\%CO_2/N_2$, (b) $20\%H_2O/N_2$.

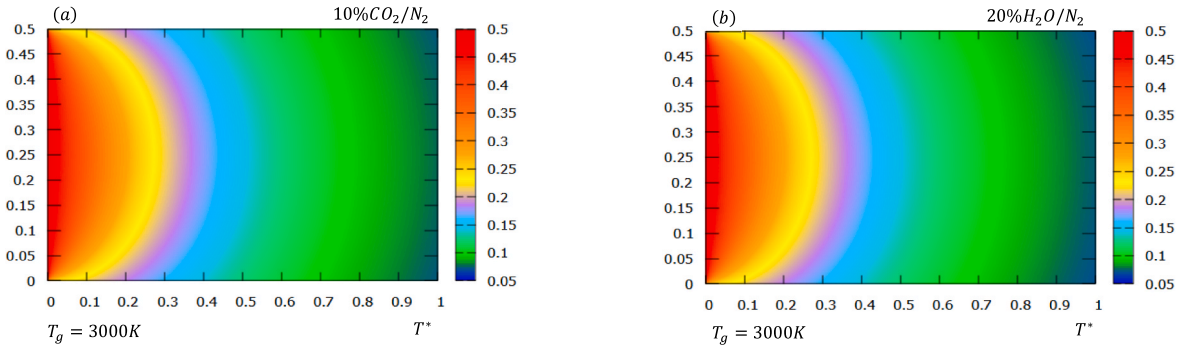

Fig. 20. Dimensionless temperature distribution T^* computed for $T_g = 3000K$: (a) $10\%CO_2/N_2$, (b) $20\%H_2O/N_2$.

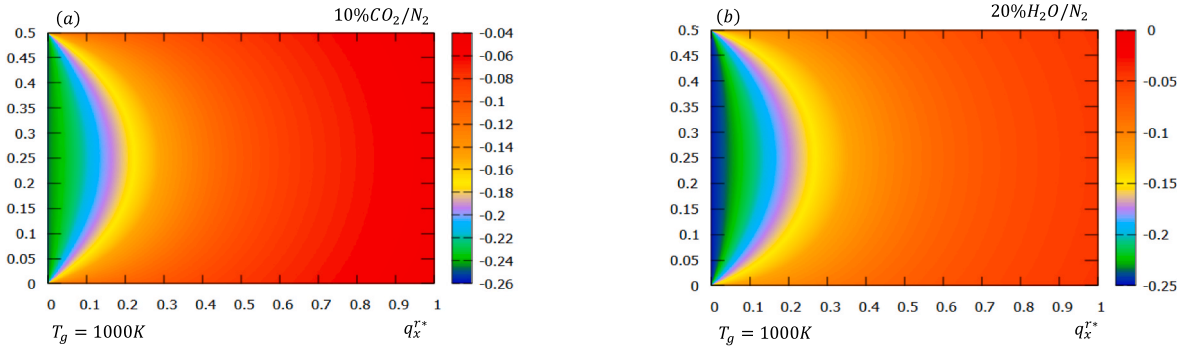

Fig. 21. x-component of dimensionless radiative heat flux $q_x^{r^*}$ computed for $T_g = 1000K$: (a) $10\%CO_2/N_2$, (b) $20\%H_2O/N_2$.

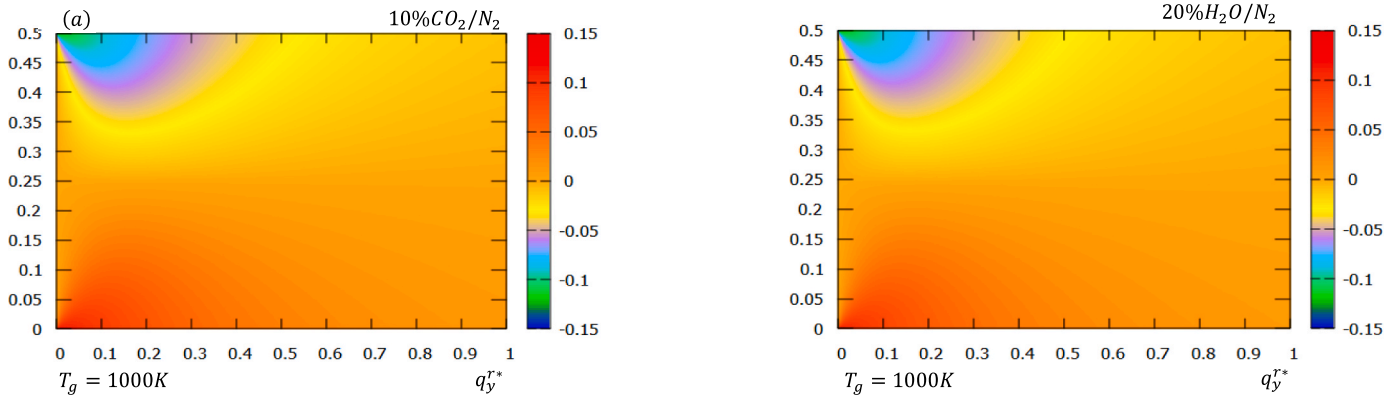

Fig. 22. y-component of dimensionless radiative heat flux $q_y^{r^*}$ computed for $T_g = 1000K$: (a) $10\%CO_2/N_2$, (b) $20\%H_2O/N_2$.

5.3.2.4. Radiative heat flux at walls: radiative equilibrium ($S^{r^*} = 0$). The plots in Fig. 15(a and b), Fig. 16(a and b) and Fig. 17(a and b), depict the radiative heat flux profiles along the North and East walls of the rectangular geometry for the respective gases. Computations have been conducted at $T_g \in \{500K, 1000K, 3000K\}$ to highlight the behavior of radiative heat flux under cold, hot, and very hot gas conditions. For $T_g = 500K$, the radiative heat flux profiles along the North wall in Fig. 15-(a), are more similar in shape than those along the East wall in Fig. 15-(b). Fig. 15-(b) shows that the radiative heat flux computed for $10\%CO_2/N_2$ exceeds that of $20\%H_2O/N_2$. When the gas temperature increases to $T_g = 1000K$, Fig. 16-(a) and Fig. 16-(b) show curves with shapes similar to those at $T_g = 500K$. Furthermore, increasing the gas temperature results in increasingly similar curve profiles, while the radiative heat flux magnitude changes only slightly.

For $T_g = 3000K$, the radiative heat flux magnitudes for $10\%CO_2/N_2$ and $20\%H_2O/N_2$ are comparable along both the North and East walls, like shown in Fig. 17(a and b). Thus, at very high temperatures, the absorption spectral bands of carbon dioxide and water vapor converge in magnitude.

5.3.3. Numerical simulations

This sub-section aims to highlight and analyse the behavior of key numerical simulations of dimensionless temperature ($T^* = T/T_{hot}$) and radiative heat flux distributions $\left(q_x^{r^*}, q_y^{r^*}, q^{r^*}\right)$ within the rectangular geometry. The chemical compositions of gases, with $Y_{CO_2} = 0.1$ and $Y_{H_2O} = 0.2$, at $T_g = T_b = 1000K$, have been used in the simulations. The West wall (Γ_W) has been maintained at hot temperature $T_W = T_{hot}$, while the other walls and the initial temperature have been set cold, such that

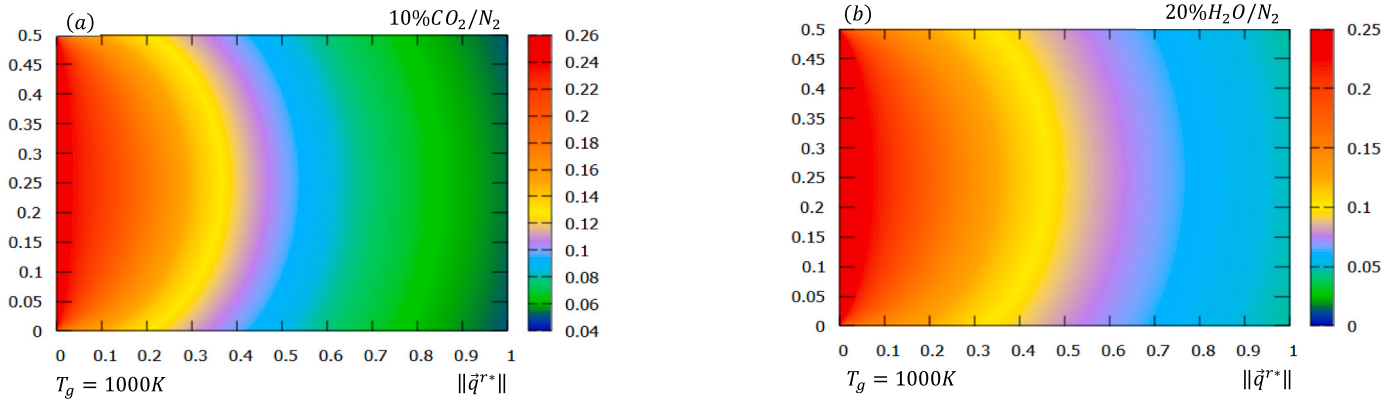

Fig. 23. Dimensionless net radiative heat flux $\|\vec{q}^{r^*}\|$, computed for $T_g = 1000K$: (a) $10\%CO_2/N_2$, (b) $20\%H_2O/N_2$.

$T_N = T_S = T_E = T_N = T_0 = T_{hot}/2$. Indeed, the computations have been carried out using an iterative scheme until convergence. To obtain detailed insight and accurately delineated contours of radiative transfer, a mesh grid of $N_x \times N_y = 1001 \times 1001$ and discrete angles of $M_\varphi \times N_\theta = 6 \times 6$, have been applied.

- *Numerical simulations of temperature distribution*

The respective numerical simulations in Fig. 18(a and b), Fig. 19(a and b) and Fig. 20(a and b) effectively depict the temperature distribution in the participating medium, for gas temperatures $T_g \in \{500K, 1000K, 3000K\}$. Temperature appears to spread more easily in a medium filled with carbon dioxide than in one filled with water vapor. For both gas species, the medium remains optically thick at a gas temperature of $T_g = 500K$, but becomes optically thin as T_g rises to $T_g = 3000K$.

For engineering applications involving extremely high operating temperatures, the temperature contours for carbon dioxide closely approach those of water vapor. Once the temperature contours at radiative equilibrium are obtained, the *x*- and *y*-components of the net radiative heat flux are highlighted.

- *Numerical simulations of radiative heat flux*

Fig. 21(a and b), Fig. 22(a and b) and Fig. 23(a and b) highlights the radiative heat flux contours of carbon dioxide and water vapor at $T_g = 1000K$. The respective numerical simulations represent a high-temperature medium. A slight difference in magnitude is observed between the contour lines of the *y*-component of the radiative heat flux for the two gas species. In contrast, the net radiative heat flux differs significantly in magnitude between carbon dioxide and water vapor. Similar trends are observed in numerical simulations at $T_g = 500K$ and $T_g = 3000K$, although they are not displayed here for convenience.

6. Conclusion

A detailed investigation of the SLW correlated model applied to carbon dioxide (CO_2/N_2), water vapor (H_2O/N_2) non-gray gases and their mixture ($CO_2/H_2O/N_2$), combined with the radiative heat transfer equation has been conducted. Nitrogen (N_2) primarily serves as a spectral window and as an oxidizer for the participating gases. The radiative integral solutions associated to the problem were accurately computed using the Gauss quadratures, the specific Bickley-Naylor functions and the ray tracing method. The numerical results for the radiative source along the centerline of the rectangular geometry, as well as the heat flux at walls, have been validated and discussed under constant temperature conditions. Radiative properties, including the discrete and Planck-mean absorption coefficients of the respective participating gases, have been calculated and tabulated for a set of gas temperatures. The influence of both the number of discrete gray gases and the temperature inside the medium have been analysed and discussed. The impact of using discrete absorption coefficients instead of the Planck-mean absorption coefficient on the dimensionless incident radiation at radiative equilibrium, has been demonstrated. Dimensionless profiles of radiative heat flux along the West and North walls, as well as the effects of the discrete angle formulation and the mesh grid used to solve the RTE, have been highlighted and discussed. Suitable numerical simulations of dimensionless temperature and heat flux distributions for the geometry section, have been performed. Thus, the assessment of thermal quantities associated with non-gray gases through exact semi-analytical and ray-tracing methods produces satisfactory results. Radiative quantities calculated with the Planck-mean absorption coefficient demand significantly less CPU time than those obtained with discrete gray absorption coefficients. The future directions of this study will address non-isothermal gas temperatures and integrate the radiative problem with conduction. The assumption of diffuse and reflective walls will likewise be considered.

CRediT authorship contribution statement

Julien Sorel Djeumegni: Writing – original draft, Methodology, Conceptualization. **Myriam Lazard:** Supervision, Funding acquisition. **Vital Le Dez:** Validation, Formal analysis.

Declaration of competing interest

The authors declare that they have no known competing financial interests or personal relationships that could have appeared to influence the work reported in this paper.'Declarations of interest: none'

Acknowledgment

This work was partially funded by the French “investments for the future” program managed by the National Agency for Research (ANR) under contract ANR-10-LABX-22-01 (Labex SOLSTICE) and supported by CNRS-Institut Pprime-University of Poitiers-ENSMA, UPR 3346; University of Nantes, ONIRIS, CNRS, GEPEA, UMR-6144.

Appendix A. Annex 1

Table A.1

• H_2O	$F_w(C,T_g,T_b,Y_w) = \frac{1}{2}tanh\left[P_w\left(T_g,T_b,\xi-\xi_p\right)\right]+\frac{1}{2}$
	$P_w\left(T_g,T_b,\xi-\xi_p\right) = \sum_{l=0}^{3}\sum_{m=0}^{3}\sum_{n=0}^{3} b_{lmn}\left(\frac{T_g}{2500}\right)^n\left(\frac{T_b}{2500}\right)^m\left(\xi-\xi_p\right)^l$
	$\xi_p = \sum_{l=0}^{3}\sum_{m=0}^{3}\sum_{n=0}^{3} u_{lmn}\left(\frac{T_gT_b}{2500^2}\right)^n\xi^m\psi_w^{l+1}$
	$\psi_w = \frac{1}{10}ln(100p_e)$
	$p_e = (1+8.17Y_w)p$
	$\xi = ln(C)\ ,\ 1.10^{-4}\le C\le 60\ \left[\frac{m^2}{mol}\right]$

Table A.2

• CO_2	$F_c(C,T_g,T_b) = \frac{1}{2}tanh\left[P_c\left(T_g,T_b,\xi-\xi_p\right)\right]+\frac{1}{2}$
	$P_c(T_g,T_b,\xi) = \sum_{l=0}^{3}\sum_{m=0}^{3}\sum_{n=0}^{3} d_{lmn}\left(\frac{T_g}{2500}\right)^n\left(\frac{T_b}{2500}\right)^m\left(\xi-\xi_p\right)^l$
	$\xi_p = \sum_{l=0}^{3}\sum_{m=0}^{3}\sum_{n=0}^{3} v_{lmn}\left(\frac{T_gT_b}{2500^2}\right)^n\xi^m\psi_c^{l+1}$
	$\psi_c = \frac{1}{10}ln(100p)$
	$\xi = ln(C)\ ,\ 1.10^{-4}\le C\le 600\ \left[\frac{m^2}{mol}\right]$

Correlation coefficients b_{lmn}, c_{lmn} and d_{lmn} are computed at atmospheric pressure, whereas u_{lmn}, v_{lmn} and w_{lmn} at variable pressure conditions and available following the link http://albdf.byu.edu

Appendix B. Annex 2

Series expansion of the first and second order Bickley-Naylor functions: $n = 1,2$

$$Ki_1(u) = \frac{\pi}{2}+u\left(\gamma+ln\left(\frac{u}{2}\right)\right)\sum_{k=0}^{\infty}\frac{\left(u^2/4\right)^k}{(k!)^2(2k+1)}-u\sum_{k=0}^{\infty}\frac{\left(u^2/4\right)^k}{(k!)^2(2k+1)^2}-x\sum_{k=0}^{\infty}\frac{\left(u^2/4\right)^kH_k}{(k!)^2(2k+1)}.$$

$$Ki_2(u) = 1-\frac{\pi}{2}u-\frac{u^2}{2}\left(\gamma+ln\left(\frac{u}{2}\right)\right)\sum_{k=0}^{\infty}\frac{\left(u^2/4\right)^k}{k!(k+1)!(2k+1)}+\frac{u^2}{4}\sum_{k=0}^{\infty}\frac{(4k+3)\left(u^2/4\right)^k}{k!(k+1)!(2k+1)^2}+\frac{u^2}{2}\sum_{k=0}^{\infty}\frac{\left(u^2/4\right)^kH_k}{k!(k+1)!(2k+1)},$$

where $\gamma = 0.57721$, is the Euler constant and $H_k = 1+\frac{1}{2}+\frac{1}{3}+\ldots\frac{1}{k}$.

Bickley-Naylor functions also follow the recurrence relationship below:

$nKi_{n+1}(u) = (n-1)Ki_{n-1}(u)-uKi_n(u)+uKi_{n-2}(u), n\ge 2.$

Appendix C. Annex 3

Dimensionless parameters:

Space coordinates: $x^* = \frac{x}{H_x}$; $y^* = \frac{y}{H_x}$.

Temperatures: $T^* = \frac{T^4}{T_{hot}^4}$; $T_0^* = \frac{T_0^4}{T_{hot}^4}$.

Radiative quantities: $G^* = \frac{G}{4\sigma_BT_{hot}^4}$; $q^{r^*} = \frac{q^r}{4\sigma_BT_{hot}^4}$ and $S^{r^*} = \frac{S^r}{4\sigma_BT_{hot}^4}$.

Data availability

The data that has been used is confidential.

References

[1] H. Chu, F. Liu, H. Zhou, Calculations of gas thermal radiation transfer in one-dimensional planar enclosure using LBL and SNB models, Int. J. Heat Mass Transf. 54 (2011) 4736–4745, https://doi.org/10.1016/j.ijheatmasstransfer.2011.06.002.

[2] R. Siegel, J.R. Howell, Thermal Radiation Heat Transfer, fourth ed., Taylor & Francis, New York, 2002.

[3] M.F. Modest, Radiative Heat Transfer, third ed., Academic Press, New York, 2013, pp. 229–246, https://doi.org/10.1016/C2010-0-65874-3.

[4] F. André, C. Calliot, V. Eymet, V. Solovjov, Rayonnement des gaz: Des Spectres De Raies Aux Modèles En k-distributions, *Ecole Thématique CNRS ETR2017* « Rayonnement Thermique en Milieux Semi-Transparents», 2017, https://doi.org/10.13140/RG.2.2.18900.40329.

[5] L. Pierrot, A. Soufiani, J. Taine, Accuracy of narrow-band and global models for radiative transfer in H_2O, CO_2 and H_2O-CO_2 mixtures at high temperature, J. Quant. Spectrosc. Radiat. Transf. 62 (1999) 523–548, https://doi.org/10.1016/S0022-4073(98)00125-3.

[6] V. Goutiere, F. Liu, A. Charette, An assessment of real-gas modelling in 2D enclosures, J. Quant. Spectrosc. Radiat. Transf. 64 (2000) 299–326, https://doi.org/10.1016/S0022-4073(99)00102-8.

[7] V. Goutiere, A. Charette, L. Kiss, Comparative performance of nongray gas modeling techniques, Numer. Heat. Transf., Part B: Fundamentals 41 (2002) 361–381, https://doi.org/10.1080/104077902753541069.

[8] H. Chu, F. Liu, H. Zhou, Calculations of gas radiation heat transfer in a two-dimensional rectangular enclosure using the line-by-line approach and the statistical narrow-band correlated-k model, Int. J. Therm. Sci. 59 (2012) 66–74, https://doi.org/10.1016/j.ijthermalsci.2012.04.003.

[9] J. Taine, A line-by-line calculation of low-resolution radiative properties of CO_2-CO-transparent nonisothermal gases mixtures up to 3000K, J. Quant. Spectrosc. Radiat. Transf. 30 (1983) 371–379, https://doi.org/10.1016/0022-4073(83)90036-5.

[10] L. Sparks, Efficient line-by-line calculation of absorption coefficients to high numerical accuracy, J. Quant. Spectrosc. Radiat. Transf. 57 (1997) 631–650, https://doi.org/10.1016/S0022-4073(96)00154-9.

[11] L.S. Rothman, I.E. Gordon, R.J. Barber, H. Dothe, R.R. Gamache, A. Goldman, V. I. Perevalov, S.A. Tashkun, J. Tennyson, HITEMP, the high-temperature molecular spectroscopic database, J. Quant. Spectrosc. Radiat. Transf. 111 (2010) 2139–2150, https://doi.org/10.1016/j.jqsrt.2010.05.001.

[12] A. Soufiani, J. Taine, High temperature gas radiative property parameters of statistical narrow-band model for H_2O, CO_2 and CO, and correlated-K model for H_2O and CO_2, Int. J. Heat Mass Transf. 40 (1997) 987–991, https://doi.org/10.1016/0017-9310(96)00129-9.

[13] M. Cherifi, S.L. Meftah, A. Benbrik, Modeling of radiative heat transfer of real gas in 2D enclosure. International Conference on Industrial Engineering and Operations Management, Bali, Indonesia, January .

[14] H. Amiri, K. Lari, Comparison of global radiative models in two-dimensional enclosures at radiative equilibrium, Int. J. Therm. Sci. 104 (2016) 423–436, https://doi.org/10.1016/j.ijthermalsci.2016.01.020.

[15] Y. Sun, X. Zhang, J.R. Howell, Non-gray combined conduction and radiation heat transfer by using FVM and SLW, J. Quant. Spectrosc. Radiat. Transf. 197 (2017) 51–59, https://doi.org/10.1016/j.jqsrt.2016.10.022.

[16] Y. Yang, S. Zheng, Q. Lu, Numerical solutions of non-gray gases and particles radiative transfer in three-dimensional combustion system using DRESOR and SNBCK, Int. J. Therm. Sci. 161 (2021) 106783, https://doi.org/10.1016/j.ijthermalsci.2020.106783.

[17] P.J. Coelho, Numerical simulation of radiative heat transfer from non-gray gases in three-dimensional enclosures, J. Quant. Spectrosc. Radiat. Transf. 74 (2002) 307–328, https://doi.org/10.1016/S0022-4073(01)00249-7.

[18] J.T. Pearson, B.W. Webb, V.P. Solovjov, J. Ma, Updated correlation of the absorption line blackbody distribution function for H2Obased on the HITEMP2010 database, J. Quant. Spectrosc. Radiat. Transf. 128 (2012) 10–17, https://doi.org/10.1016/j.jqsrt.2012.07.016.

[19] J.T. Pearson, B.W. Webb, V.P. Solovjov, J. Ma, Efficient representation of the absorption line blackbody distribution function for H2O, CO2, and COat variable temperature, mole fraction, and total pressure, J. Quant. Spectrosc. Radiat. Transf. 138 (2014) 82–96, https://doi.org/10.1016/j.jqsrt.2014.01.019.

[20] J.S. Djeumegni, M. Lazard, V. Le Dez, H.T.T. Kamdem, Modeling of radiative heat transfer in a gray semi-transparent medium with internal fluid cavity limited by black boundary surfaces, TI-Int. J. Eng. Sci. 63 (2019) 205–210, https://doi.org/10.18280/ti-ijes.632-413.

[21] J.S. Djeumegni, M. Lazard, V. Le Dez, H.T.T. Kamdem, Radiative heat transfer in a 2D semi-transparent gray medium with a centered inner square cavity, Int. J. Heat Mass transf. 149 (2020) 119209, https://doi.org/10.1016/j.ijheatmasstransfer.2019.119209.

[22] Z. Altaç, Integrals involving bickley and bessel functions in radiative transfer, and generalized exponential integral functions, ASME J. Heat Transf. 118 (1996) 789–791, https://doi.org/10.1115/1.2822701.

[23] H.C. Hottel, A.F. Sarofim, Radiative Transfer, McGraw-Hill Book Company, New York, 1967.

[24] M.K. Denison, B.W. Webb, A spectral line-based weighted-sum-of-gray-gases model for arbitrary RTE solvers, ASME J. Heat Transf. 115 (1993) 1004–1012, https://doi.org/10.1115/1.2911354.

[25] M.K. Denison, B.W. Webb, An absorption-line blackbody distribution function for efficient calculation of total gas radiative transfer, J. Quant. Spectrosc. Radiat. Transf. 50 (1993) 499–510, https://doi.org/10.1016/0022-4073(93)90043-H.

[26] M. Darbandi, B. Abrar, Thermal radiation transfer calculations in combustion fields using the SLW model coupled with a modified reference approach, J. Quant. Spectrosc. Radiat. Transf. 205 (2018) 105–113, https://doi.org/10.1016/j.jqsrt.2017.08.023.

[27] M.F. Modest, S. Mazumder, Radiative Heat Transfer, fourth ed., Academic Press: McGraw-Hill, 2021, pp. 657–736, https://doi.org/10.1016/C2018-0-03206-5.

[28] R.J. Hargreaves, I.E. Gordon, X. Huang, G.C. Toon, L.S. Rothman, Updating the carbon dioxide line list in HITEMP, J. Quant. Spectrosc. Radiat. Transf. 333 (2025) 109324, https://doi.org/10.1016/j.jqsrt.2024.109324.

[29] I.E. Gordon, L.S. Rothman, R.J. Hargreaves, R. Hashemi, E.V. Karlovets, F. M. Skinner, et al., The HITRAN2020 molecular spectroscopic database, J. Quant. Spectrosc. Radiat. Transf. 277 (2022) 107949.

[30] M.F. Modest, H. Zhang, The full-spectrum correlated-k distribution for thermal radiation from molecular gas-particulate mixtures, ASME J. Heat Transf. 124 (2002) 30–38, https://doi.org/10.1115/1.1418697.

[31] H. Zhang, M.F. Modest, A multi-scale full-spectrum correlated-*k* distribution for radiative heat transfer in inhomogeneous gas mixtures, J. Quant. Spectrosc. Radiat. Transf. 73 (2002) 349–360, https://doi.org/10.1016/S0022-4073(01)00220-5.

[32] V. Le Dez, H. Sadat, Radiative heat transfer in a semi-transparent medium enclosed in a two-dimensional square cavity, J. Quant. Spectrosc. Radiat. Transf. 112 (2011) 847–863, https://doi.org/10.1016/j.jqsrt.2010.11.008.